Coupled Wavelength Postbuckling Analysis of Composite Laminates under Compression and Shear

Kai Zhao[a], David Kennedy[a], Carol A. Featherston[a], Xiaoyang Liu[b,*]

[a] *School of Engineering, Cardiff University, Queen's Buildings, The Parade, Cardiff CF24 3AA, U.K.*

[b] *School of Civil Engineering, Qingdao University of Technology, Qingdao 266033, China*

* Corresponding author. Email liuxiaoyang@qut.edu.cn (X. Liu)

Abstract

This paper introduces a novel approach, the coupled wavelength postbuckling analysis (CWPAN), to study the postbuckling behaviour of composite laminates under various conditions. CWPAN utilizes sinusoidal solutions, derived from the exact strip method, to represent in-plane displacements, strains, and stresses, reducing the size of the stiffness matrix, and thereby the computational expense. To handle progressive out-of-plane displacements along the postbuckling path, a novel Newton iteration scheme, based on the Exact Strip Method, is employed. By transforming nonlinear equations into linear ones, CWPAN maintains stability for postbuckling nonlinearities. The efficacy and efficiency of CWPAN is illustrated by comparisons with finite element method.

Keywords: Postbuckling; composite laminates; exact strip method; shear load; compression load.

1. Introduction

Composite laminates have the reserve of postbuckling strength, surpassing the initial critical buckling load [1]. This capability allows aircraft design to achieve further weight reduction by effectively utilizing the inherent stability of the postbuckling phase [2].

In the preliminary design phase of an aircraft, structural design is focused on developing an airframe that optimally balances weight, strength, and stiffness. It involves the use of computational modelling, like Finite Element analysis (FEA), to predict the response of the structures, such as the fuselage, wings, and empennage—to various stresses encountered across different flight conditions. However, the preliminary design stage requires less detailed analysis but needs to consider many candidate configurations and load cases [3]. It can therefore benefit from the use of alternative, simpler yet reliable forms of analysis which are faster than the FE method, in terms of both modelling and computational time [4]. In recent years, IsoGeometric analysis has been studied extensively. It presents no geometric approximation error, due to the fact the domain is represented exactly [5,6]. However,

the conditioning of system matrices is one of the drawbacks of Generalized/eXtended IsoGeometric Analysis (GIGA/XIGA), which results in increase in computational cost in the case of iterative solvers or erroneous results in the case of direct solvers. Analytical solutions provide precise prediction of buckling and postbuckling behaviour which is crucial for optimizing in preliminary design. However, it has limitations in handling complex geometries, material anisotropy and the nonlinearities, resulting in simplification along with the sacrifice of the accuracy [7]. The semi-analytical method, on the other hand, is a balance between computational efficiency and the accuracy of results. By integrating analytical approaches with numerical techniques, this method can handle complex boundary conditions and geometrical nonlinearities more effectively than purely analytical methods [8].

Research on the semi-analytical method has been conducted for several decades. For example, Bisagni et al. [9] introduced formulations to study the buckling and postbuckling behaviour of isotropic stiffened panels under compressive loads analytically. By employing the Ritz method, they approached the localized postbuckling problem using non-linear governing equations and trigonometric shape functions [10]. Subsequently, the authors further enhanced the postbuckling analysis [11], extending its applicability to include curved stiffened panels and combined loading scenarios. Raju et al. [12] established equilibrium equations using first-order shear deformation theory for postbuckling analysis in variable angle tow composites and functionally graded plates. By employing the differential quadrature method (DQM), their work was then extended by introducing a postbuckling analysis technique [12,13], specifically tailored for variable angle tow composite plates subjected to in-plane shear. Li et al. [11] introduced the element-free Galerkin approach tailored for analysing the postbuckling behaviour of composite plates with circular cut-outs featuring variable stiffness. Chen and Qiao [14] delved into postbuckling analysis for composite plates under shear with rotational restraints, employing a Galerkin-based method. Wang et al. [15] conducted an experimental work to investigate the postbuckling behaviour of stiffened composite laminates, and based on the test results, a rapid postbuckling analysis method using interaction formulas was developed and validated. In the work of Bouslama et al. [16], both experimental and numerical studies were performed on postbuckling responses of stiffened composite laminates, and a progressive failure analysis method was developed and demonstrated accurate predictions of the out-of-plane displacements and deflection shape. Shojaee et al. [17] experimentally investigated the buckling and postbuckling behaviour of composite laminates with cutouts, and a semi-energy finite strip method was proposed based on the first-order shear theory. The results predicted by the semi-analytical method showed a good agreement with the experimental results.

The availability of a wide range of efficient and dependable postbuckling techniques have opened the door to solving progressively more intricate problems. Yet, it's worth noting that many of these techniques primarily

consist of theoretical frameworks rather than comprehensive strategies. Unfortunately, the postbuckling behaviour of composite panels remains relatively underexplored and is not fully leveraged within industrial applications.

The Exact Strip Method (ESM) is a semi-analytical method [18] for buckling and natural frequency analysis for prismatic plate assemblies. In this method, the buckling modes of composite plates are presumed to be sinusoidal variation along the plates' longitudinal direction. Wittrick and Williams [19–21] formulated an algorithm to address the resulting transcendental eigenvalue problem. This approach allows for the derivation of exact solutions for isotropic and orthotropic panels under simply supports in the absence of shear loading. The longitudinal continuity of typical wing and fuselage panels is closely approximated because the solutions are for the infinitely long structure obtained by repeating a bay and its supports longitudinally. The method was then extended to capture skewed mode shapes that caused by laminate anisotropy and shear loads using coupled wavelengths variations [19]. Above methods have then been packed into a computer program, VICONOPT [22,23], with additional capability of optimization. Comparison with usual approximate finite-element methods confirms that, for comparably converged solutions, VICONOPT is typically between 100 and 10^4 times faster [23], which is ideal for the preliminary design. This advantage can be extended to postbuckling analysis.

The postbuckling analysis based on ESM was first introduced by Zhang [24], who used sinusoidal functions with single wavelength to analysis composite plates under compression. The work was then extended to cover composite plate under shear load using multiply wavelengths by Zhao [25]. However, both studies only predict postbuckling at a specific state, as they do not include the linear terms of shear loading and fail to account for the non-linearity of displacements. Consequently, these approaches fail to capture the growing skewed postbuckling modes and the postbuckling paths. Additionally, research by Zhao only considers fixed-edge boundary conditions, overlooking more complex scenarios.

This paper presents a new composite postbuckling technique, Coupled Wavelength Postbuckling Analysis (CWPAN), which covers not only a novel solution at each discrete postbuckling state for composite laminate under shear loads, but also a framework of convergence strategies allowing exploration along a full postbuckling path. CWPAN improves the previous work that uses sinusoidal formulations to represent in-plane displacements, strain and stresses. The governing equations for postbuckling are systematically composed and solved analytically at every postbuckling state through classical plate theory and the large deflection theory. Additionally, a convergence procedure is proposed, comprising a Newton iteration Scheme (NIS) and associated schemes, in order to effectively demonstrate the evolving postbuckling behaviour. CWPAN's efficacy is demonstrated through

practical applications, including symmetric and balanced composite laminates subject to in-plane compression, shear, or combined compression and shear, under different boundary conditions. The results are verified against the most commonly employed numerical technique, FEA.

Section 2 presents a novel approach in which sinusoidal modes are coupled to provide accurate solutions, especially applicable to anisotropic plates subjected to shear loads. Section 3 addresses issues of convergence and presents a Newton iteration scheme designed to track the postbuckling path effectively. Section 4 presents illustrative results and validation exercises to showcase the practical applicability and accuracy of the proposed method. Finally, Section 5 provides the conclusions drawn from the study.

2. In-plane solution for postbuckling analysis

The previous research on postbuckling analysis using coupled sinusoidal wave variations demonstrated that the method can accurately predict discrete postbuckling states [25]. However, to obtain continuous postbuckling paths, the approach requires to consider the linear shear terms and a systematic framework with approaches to capture displacement non-linearity.

The composite laminates in CWPAN are considered to fluctuate as a combination of multiple sinusoidal components in the longitudinal direction. Given the out-of-plane displacements by the ESM, the half-wavelengths of sinusoidal components for the in-plane solutions are derived. Next, expressions for strains, curvatures, and stress resultants are formulated based upon in-plane displacements, employing von Kármán's large deflection theory. Subsequently, in-plane equilibrium equations are formulated, adjusted in order to account for in-plane boundary conditions, and then solved to obtain in plane displacements.

This entire iterative process for postbuckling analysis at a specific level of end shortening strain is carried out analytically, as depicted in Figure 1. Further elaboration on each of these stages is provided in the subsequent sections.

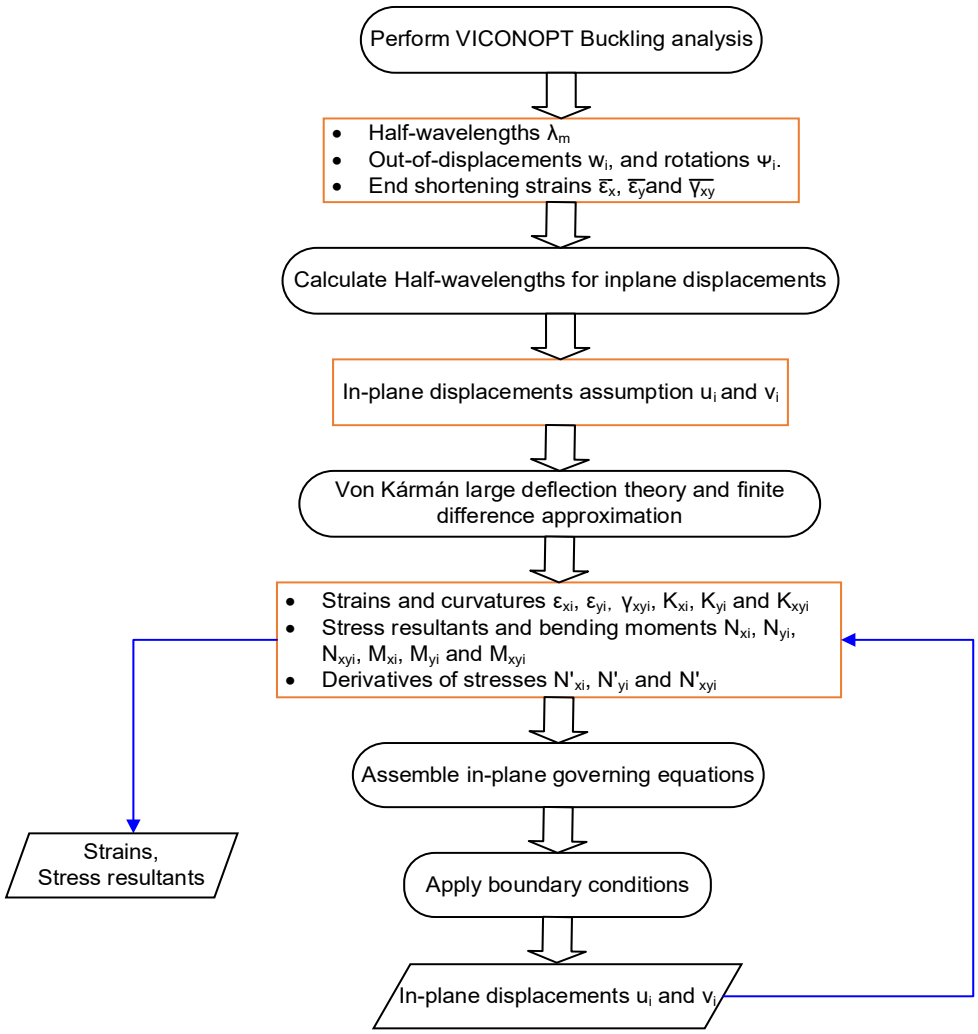

Figure 1. Calculation procedures for postbuckling analysis at each level of end shortening strain.

2.1. Displacement assumption

Following by Zhao [25], the plate is partitioned into n-1 strips, each having equal width, defined by n nodes situated at the strip boundaries, as depicted in Figure 2.

For every node i, the rotations ψ_i and the vertical deflections w_i around x axis are modelled as accumulations of sinusoidal responses in the longitudinal direction with half-wavelengths λ_m, in the following form:

$$\begin{bmatrix} w_i \\ \psi_i \end{bmatrix} = \begin{bmatrix} \sum_m w_{imc} cos\frac{\pi x}{\lambda_m} + w_{ims} sin\frac{\pi x}{\lambda_m} \\ \sum_m \psi_{imc} cos\frac{\pi x}{\lambda_m} + \psi_{ims} sin\frac{\pi x}{\lambda_m} \end{bmatrix} \quad (1)$$

where the amplitudes w_{imc}, w_{ims}, ψ_{imc} and ψ_{ims} are determined through the ESM conducted in the preceding iteration. Here, the subscript m signifies the specific set of out-of-plane half-wavelengths. In accordance with

classical plate theory, ψ_i is assumed to be equivalent to the derivative of w_i, with respect to the transverse direction y, denoted as w_i'.

Considering von Kármán's large deflection theory, computations for curvatures and strains result in expressions that involve products of trigonometric terms. These expressions can often be simplified into combinations of different trigonometric terms as described in [25]. Consequently, the in-plane displacements are represented as a series that encompasses all possible trigonometric terms arising from summations and subtractions:

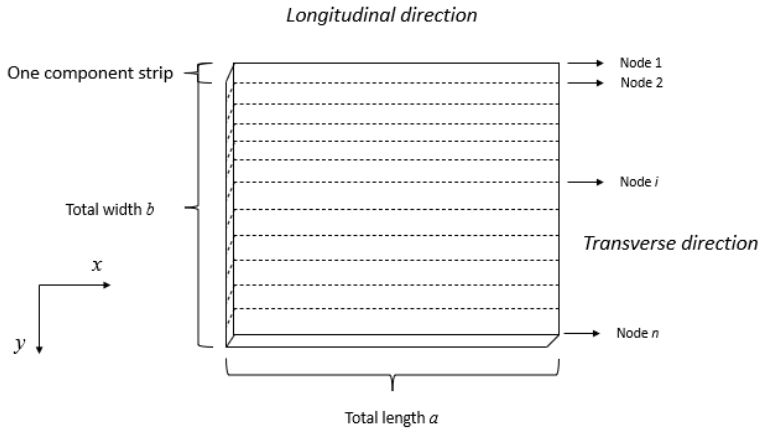

Figure 2. A plate of length a and width b divided into n-1 strips of equal width.

$$\begin{bmatrix} u_i \\ v_i \end{bmatrix} = \begin{bmatrix} \overline{\varepsilon}_x \left(x - \frac{a}{2}\right) + \overline{\gamma}_{xy} \left(y - \frac{b}{2}\right) + \sum_k u_{ikc} cos \frac{\pi x}{\lambda_k} + u_{iks} sin \frac{\pi x}{\lambda_k} \\ \overline{\varepsilon}_y \left(y - \frac{b}{2}\right) + \overline{\gamma}_{xy} \left(x - \frac{a}{2}\right) + \sum_k v_{ikc} cos \frac{\pi x}{\lambda_k} + v_{iks} sin \frac{\pi x}{\lambda_k} \end{bmatrix} \quad (2)$$

where $\overline{\varepsilon}_x$, $\overline{\varepsilon}_y$, $\overline{\gamma}_{xy}$ represent the uniform longitudinal, transverse, and shear strains progressively imposed on the plate, respectively. The subscript k signifies specific sets of in-plane half-wavelengths. a represents the length of the plate, while b corresponds to its width. Different from study by Zhao [25], the linear term for $\overline{\gamma}_{xy}$ is included to account for shear loads.

It is important to highlight that terms for linear strain are predetermined parameters, defined according to the end shortening strain observed during the initial buckling analysis. In other words, the postbuckling analysis is governed by adjusting the ratio of increments for linear strain, denoted as α, i.e. for the applied strain at critical buckling $\overline{\varepsilon}_{x0}$, the applied strain $\overline{\varepsilon}_x$ at the j^{th} postbuckling cycle will be $(1 + j\alpha)\overline{\varepsilon}_{x0}$.

This assumption closely resembles the approach used in deflection-controlled Finite Element Analysis (FEA) simulations, where the plate is subjected to progressive in-plane displacements in proportion to the applied load,

as opposed to uniform stresses or concentrated forces. It also aligns more closely with experimental practices, where controlling displacements is often more feasible than controlling loads. Performing tests under load control can introduce the risk of the testing machine accelerating if the component's stiffness decreases. In such cases, maintaining a consistent load can potentially result in accidents or even damage to the testing equipment. This concern is particularly relevant when dealing with unstable responses, such as postbuckling behaviour.

Employing this assumption ensures that the ratio between shear and elongation strains remains consistent throughout the analysis. In practical terms, if the plate experiences a combined loading scenario, the proportion of applied compressive strain to applied shear strain will persist at the same ratio as observed during the initial buckling stage throughout the entire postbuckling analysis. This offers valuable stability in the analysis process and maintains the relative behaviour of these strain components.

2.2. Strain and curvatures

In accordance with von Kármán's large deflection theory [26], the curvature and strain at node *i* can be expressed as follows:

$$\begin{bmatrix} \varepsilon_{xi} \\ \varepsilon_{yi} \\ \gamma_{xyi} \\ \kappa_{xi} \\ \kappa_{yi} \\ \kappa_{xyi} \end{bmatrix} = \begin{bmatrix} \dfrac{\partial u_i}{\partial x} + \dfrac{1}{2}\left(\dfrac{\partial w_i}{\partial x}\right)^2 \\ \dfrac{\partial v_i}{\partial y} + \dfrac{1}{2}\left(\dfrac{\partial w_i}{\partial y}\right)^2 \\ \dfrac{\partial u_i}{\partial y} + \dfrac{\partial v_i}{\partial x} + \dfrac{\partial w_i}{\partial x}\dfrac{\partial w_i}{\partial y} \\ -\dfrac{\partial^2 w_i}{\partial x^2} \\ -\dfrac{\partial^2 w_i}{\partial y^2} \\ -2\dfrac{\partial^2 w_i}{\partial x \partial y} \end{bmatrix} \tag{3}$$

Substituting from Eq. (2) into Eq. (3) and writing in vector notation gives

$$\boldsymbol{\varepsilon_i} = \boldsymbol{\varepsilon}_0(\mathbf{w}_i) + \boldsymbol{\varepsilon}_1\mathbf{u}_i + \boldsymbol{\varepsilon}_2\mathbf{f}\mathbf{u}_i$$

$$\boldsymbol{\kappa_i} = \boldsymbol{\kappa}_0(\mathbf{w}_i) \tag{4}$$

Here $\boldsymbol{\varepsilon}_0(\mathbf{w}_i)$ and $\boldsymbol{\kappa}_0(\mathbf{w}_i)$ are functions of the given out-of-plane displacements, while rotations $\mathbf{w}_i$ are derived according to von Kármán's large deflection theory. $\mathbf{u}_i$ contains unknown in-plane displacements in the directions of transverse and longitudinal. $\boldsymbol{\varepsilon}_1$, $\boldsymbol{\varepsilon}_2$, $\mathbf{f}$ denote coefficient matrices defined in the Appendix.

2.3. Equilibrium equations

Stress resultants N_{xi}, N_{yi}, N_{xyi} are essential components required to establish formulations of the equilibrium equations and complete the final analysis, formulated as follows:

$$\begin{bmatrix} N_{xi} \\ N_{yi} \\ N_{xyi} \\ M_{xi} \\ M_{yi} \\ M_{xyi} \end{bmatrix} = \begin{bmatrix} A_{i11} & A_{i12} & A_{i16} & B_{i11} & B_{i12} & B_{i16} \\ A_{i12} & A_{i22} & A_{i26} & B_{i12} & B_{i22} & B_{i26} \\ A_{i16} & A_{i26} & A_{i66} & B_{i16} & B_{i26} & B_{i66} \\ B_{i11} & B_{i12} & B_{i16} & D_{i11} & D_{i12} & D_{i16} \\ B_{i12} & B_{i22} & B_{i26} & D_{i12} & D_{i22} & D_{i26} \\ B_{i16} & B_{i26} & B_{i66} & D_{i16} & D_{i26} & D_{i66} \end{bmatrix} \begin{bmatrix} \varepsilon_{xi} \\ \varepsilon_{yi} \\ \varepsilon_{xyi} \\ \kappa_{xi} \\ \kappa_{yi} \\ \kappa_{xyi} \end{bmatrix} \tag{5}$$

Substituting Eq. (4) into Eq.(5) and using vector notation gives

$$\begin{aligned} \mathbf{N}_i &= \mathbf{A}[\boldsymbol{\varepsilon}_0(\mathbf{w}_i) + \boldsymbol{\varepsilon}_1\mathbf{u}_i + \boldsymbol{\varepsilon}_2\mathbf{f}\mathbf{u}_i] + \mathbf{B}\boldsymbol{\kappa}_0(\mathbf{w}_i) \\ \mathbf{M}_i &= \mathbf{B}[\boldsymbol{\varepsilon}_0(\mathbf{w}_i) + \boldsymbol{\varepsilon}_1\mathbf{u}_i + \boldsymbol{\varepsilon}_2\mathbf{f}\mathbf{u}_i] + \mathbf{D}\boldsymbol{\kappa}_0(\mathbf{w}_i) \end{aligned} \tag{6}$$

The derivatives of the stress resultants with respect to the transverse direction are given by

$$\mathbf{N}_i' = \mathbf{A}[\boldsymbol{\varepsilon}_0'(\mathbf{w}_i) + \boldsymbol{\varepsilon}_1\mathbf{f}\mathbf{u}_i + \boldsymbol{\varepsilon}_2\mathbf{s}\mathbf{u}_i] + \mathbf{B}\boldsymbol{\kappa}_0'(\mathbf{w}_i) \tag{7}$$

where $\mathbf{f}$ and $\mathbf{s}$ are matrices of the first and the second order derivatives of the stress resultants with respect to the transverse direction, while $\boldsymbol{\varepsilon}_0'(\mathbf{w}_i)$ and $\boldsymbol{\kappa}_0'(\mathbf{w}_i)$ contain derivatives of $\boldsymbol{\varepsilon}_0(\mathbf{w}_i)$ and $\boldsymbol{\kappa}_0(\mathbf{w}_i)$ with respect to the transverse direction, more details of which can be found in the Appendix.

In accordance with classical plate theory, the equilibrium equations are expressed as follows:

$$\frac{\partial N_{yi}}{\partial y} + \frac{\partial N_{xyi}}{\partial x} = 0 \tag{8}$$

$$\frac{\partial N_{xyi}}{\partial y} + \frac{\partial N_{xi}}{\partial x} = 0 \tag{9}$$

which can be simplified as

$$\mathbf{T}\mathbf{N}_i' + \mathbf{R}\mathbf{N}_i = 0 \tag{10}$$

where details of the $\mathbf{T}$ and $\mathbf{R}$ matrices can be found in the Appendix.

Substituting Eqs. (6) and (7) into Eq. (10),

$$[\mathbf{TA}(\boldsymbol{\varepsilon}_1\mathbf{f}+\boldsymbol{\varepsilon}_2\mathbf{s})+\mathbf{RA}(\boldsymbol{\varepsilon}_1+\boldsymbol{\varepsilon}_2\mathbf{f})]\mathbf{u}_i=-\mathbf{TA}\boldsymbol{\varepsilon}_0'(\mathbf{w}_i)-\mathbf{RA}\boldsymbol{\varepsilon}_0(\mathbf{w}_i)-\mathbf{TB}\boldsymbol{\kappa}_0'(\mathbf{w}_i)-\mathbf{RB}\boldsymbol{\kappa}_0(\mathbf{w}_i) \quad (11)$$

To determine the in-plane displacements $\mathbf{u}_i$, Eq. (11) can be simplified as follows:

$$\mathbf{L}\mathbf{u}_i=\mathbf{H}(\mathbf{w}_i) \quad (12)$$

Thus $\mathbf{u}_i$ can be expressed as

$$\mathbf{u}_i=\mathbf{L}^{-1}\mathbf{H}(\mathbf{w}_i) \quad (13)$$

L in Eq. (12) is a square matrix related only to the constant properties of the plate, while $\mathbf{H}(\mathbf{w}_i)$ represents non-linear functions of vertical displacements which vary throughout postbuckling. To prevent redundant calculations, the matrix **L** is constructed and inverted prior to commencing the postbuckling analysis. Consequently, whenever there is a need to solve the equilibrium equations, the in-plane displacements $\mathbf{u}_i$ can be readily determined by performing the matrix multiplication described in Eq. (13).

2.4. Boundary and loading conditions

In this paper, it is assumed that all four edges of the plate are constrained against out-of-plane displacement, meaning that $w=0$ along these edges. Three different in-plane boundary conditions are considered for the longitudinal edges:

For the free edge case, all four edges of the plate are permitted to undergo in-plane movements and rotations, as depicted in Figure 3(left) where black strips signify the presence of rigid bodies that exert control over the displacements of the structure. Consequently, stress resultants $\mathbf{N}_x$, $\mathbf{N}_y$ are both zero at the longitudinal edges and the equilibrium equations at these edges are replaced by the constraint equations

$$\mathbf{N}_{x1}=0;\ \mathbf{N}_{xn}=0;\ \mathbf{N}_{y1}=0;\ \mathbf{N}_{yn}=0 \quad (14)$$

Fixed boundary conditions are characterized by displacement constraints imposed on all components in the transverse direction, namely $\mathbf{u}_1\neq 0$, $\mathbf{u}_n\neq 0$, $\mathbf{v}_1=0$ and $\mathbf{v}_n=0$, as shown in Figure 3(middle). As a result, $\mathbf{N}_x$ at the longitudinal edges is zero, and their equilibrium equations are replaced by specific constraint equations:

$$\mathbf{N}_{x1}=0;\ \mathbf{v}_1=0;\ \mathbf{N}_{xn}=0;\ \mathbf{v}_n=0 \quad (15)$$

For the straight edges, the longitudinal edges maintain a straight configuration while moving toward or away from each other, as shown in Figure 3(right). Consequently, certain conditions follow: the constant displacement terms are nonzero, $v_{1,0}\neq 0$; $v_{n,0}\neq 0$, constant terms for stress are 0, $N_{x1,0}=0$, $N_{xn,0}=0$ and other amplitudes along

188 the boundaries, corresponding to the sinusoidal components, are set to 0. Given that the boundaries in the
189 longitudinal direction can move freely, the corresponding equilibrium equations are written as:

$$\mathbf{N}_{x1} = 0 \text{ and } \mathbf{N}_{xn} = 0 \tag{16}$$

190 To prevent rigid body movement, various options can be considered, as equations for constant components of the
191 displacements $u_{i,0}$ are singular. One efficient approach is to set one of these equations to zero. However, for
192 symmetry preservation, the equations corresponding to the first and last nodes are replaced with $u_{1,0} = 0$ and
193 $u_{n,0} = 0$ respectively. Another possibility is to set the displacements at the middle node to zero. However, since
194 this constrains the middle node in its displacements in both directions, it can introduce unnecessary constraints
195 and potentially result in less accurate solutions. Regarding the boundary conditions in the lateral direction, point
196 supports can be applied at any location on the plate through the VICONOPT analysis (in the first cycle) or the
197 modified Newton iteration scheme (in the subsequent cycles). This flexibility allows for tailored adjustments to
198 address specific analysis needs.

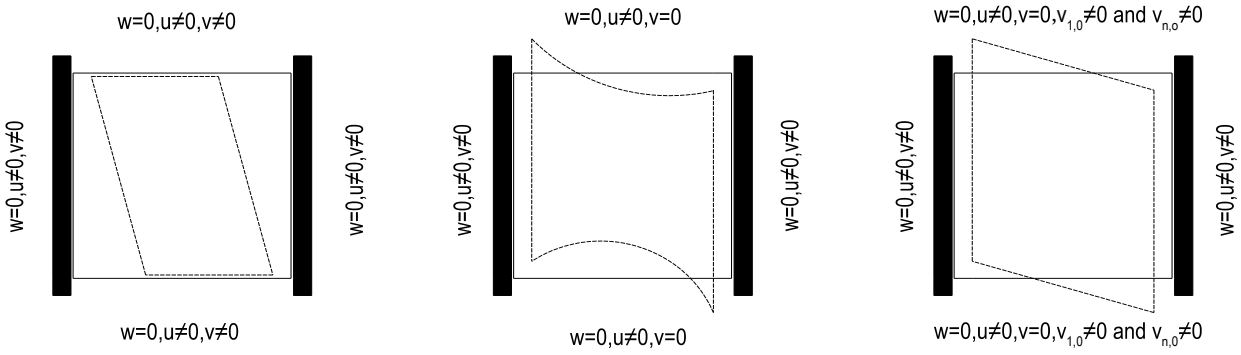

199

200 Figure 3. Free boundary condition (left); b. fixed boundary condition (middle); c. straight boundary condition
201 (right).

202 In each of these boundary condition scenarios, the equilibrium equations are formulated to determine
203 displacements *u* and *v*. By substituting these displacements back into Eqs. (4) and (6), the stress resultants and
204 strains are derived (stress resultants can also be obtained by substituting strains into Eq. (6)). Since all of the
205 solutions are trigonometric terms at node level, they must be summed to obtain the actual values at a specific
206 location.

207 Solving Eqs. (8) and (9) involves the calculation of the derivatives of the stress resultants N_x, N_y, N_{xy}. These
208 stress resultants comprise constants, N_{x0}, N_{y0} and N_{xy0}, as well as sinusoidal terms based on the half-wavelengths

derived from the initial calculation, see Eq. (9). The constant terms are formed primarily by the end shortening strain $\overline{\varepsilon}_x$ with or without the inclusion of any shear strain $\overline{\gamma}_{xy}$, both of which constitute the most substantial contribution to the in-plane displacements. However, it is worth noting that these terms are solely used to solve the sinusoidal parts of in-plane displacements (i.e., the varying components of the displacements), i.e. they are not involved in the equilibrium equations. This is because the linear terms involving end shortening strain are of first order, whereas the strains and stresses in the equilibrium equations are based on second-order derivatives.

To determine the in-plane displacements, results derived by resolving the equilibrium equations must include the reintroduction of end shortening into Eq. (5) according to the specific location within the structure. Likewise, when substituting *u* and *v* into Eq. (6) and (8), it is crucial to incorporate end shortening strain and shear strain into the formulation for actual strain. Consequently, this procedure yields distributions of in-plane and out-of-plane displacements, strains, and stresses. Throughout the remainder of this paper, this process will be referred to as the "in-plane solution."

3. Postbuckling analysis framework

3.1. Convergence procedure

In CWPAN, the applying loads can be in-plane compression, pure shear, or compression and shear. The materials of the plates can be isotropic, or anisotropic symmetric laminated composite. The analysis consists of multiple cycles, each defined by a predetermined increment/step of longitudinal strain with or without shear strain. At every cycle, by solving the equilibrium equations, various aspects are determined including the external loadings, distribution of stresses and shapes and amplitudes of the postbuckling mode, as depicted Figure 4.

The postbuckling mode shape plays a crucial role in the in-plane calculations because it serves as a known quantity within those solutions. To account for the evolving postbuckling mode in each cycle, a Newton iteration Scheme (NIS) is employed. The trial out-of-plane displacements for the first cycle are initially determined through a VICONOPT initial buckling analysis. This information is then used as a starting point for subsequent iterations to capture the changing postbuckling mode at each cycle.

Consider plates with critical buckling loads, P_{cr}, longitudinal end shortening strain, ε_0 and shear strain γ_0. At the *m*th iterative cycle, the longitudinal end shortening will be $\varepsilon_m = (1 + m\alpha)\varepsilon_0$ and the shear strain will be $\gamma_m = (1 + m\alpha)\gamma_0$, where α is the postbuckling increment ratio. It is important to note that, as previously mentioned, the ratio between the end shortening strain ε_m and the shear strain γ_m remains consistent with the ratio at the

point of initial buckling. By incorporating ε_m, γ_m and the out-of-plane displacements obtained through convergence in the NIS into the in-plane solutions, it is possible to ascertain in-plane displacements, stresses and strains for the present cycle. This process allows for the analysis of the plate's behavior as it undergoes progressive postbuckling.

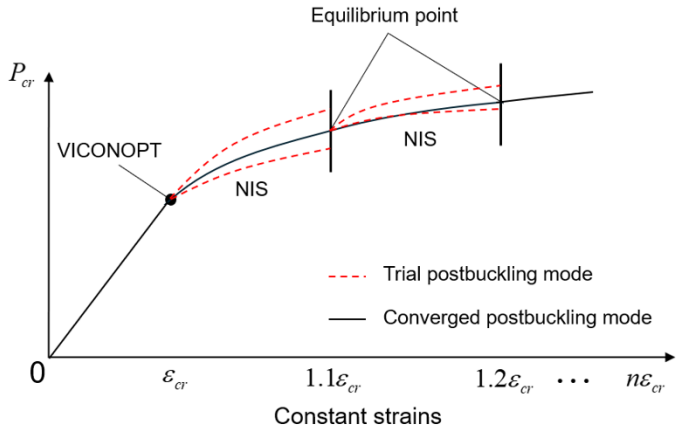

Figure 4. Illustration of the postbuckling analysis procedure ($\alpha = 0.1$).

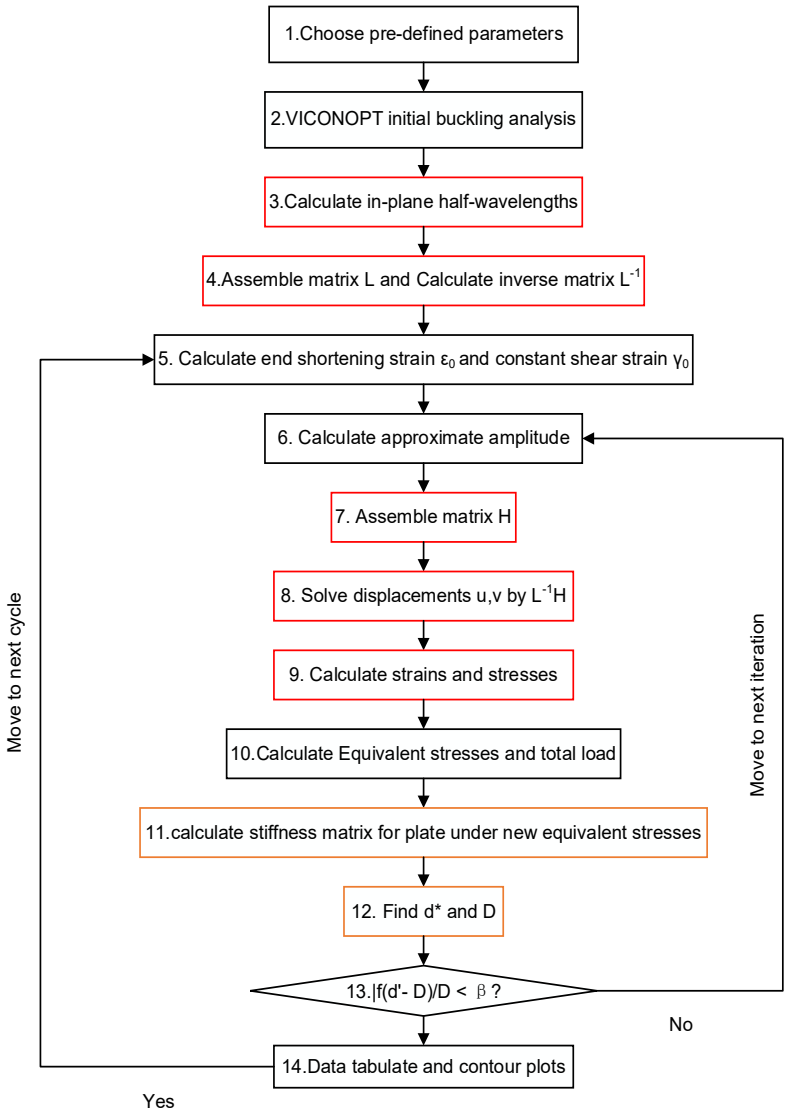

Figure 5. Convergence strategy showing proposed postbuckling analysis.

In the second and subsequent cycles, a different approach is taken. Instead of applying a uniform compressive load P, equivalent stress resultants are applied to each longitudinal strip to account for the effects of stress redistribution that occur as the plate undergoes postbuckling behavior. This iterative process leads to the determination of a new buckling load P_{cr} and the corresponding out-of-plane displacements for each iterative cycle. By following this process, a comprehensive postbuckling analysis is carried out, as demonstrated in the flow chart presented in Figure 5. Each step is now elaborated as follows:

1. Four pre-determined parameters are required.

(i) The number of half-wavelengths for out-of-plane expressions, denoted as k. Increasing this number theoretically leads to more accurate solutions, but it significantly increases computational complexity and time,

seen from Eqs. (1) - (13). Therefore, choosing an appropriate value for k is crucial to balance accuracy and computational efficiency.

(ii) The number of nodes, denoted as n. This parameter is akin to the mesh in Finite Element Analysis (FEA), i.e. a higher number of nodes increases accuracy but reduces computational efficiency.

(iii) The increment ratio of longitudinal end shortening and shear strains, α, which is equivalent to the step size in FEA. Selecting an appropriate α value is critical, especially for challenging cases such as composite plates under pure shear. A large α may lead to difficulties in capturing mode changes in the Newton iteration scheme.

(iv) The convergence tolerance for the NIS, denoted as β, Typically set to 0.1%, this parameter controls the convergence criteria for the iteration process.

2. Initiation of the analysis commences via VICONOPT for buckling using plate properties and predetermined parameters. Outputs from the VICONOPT analysis include vertical displacements, rotations, initial end shortening and shear strains and the buckling load.

3. Using the known half-wavelengths, in-plane half-wavelengths are determined according to von Kármán's large deflection theory.

4. Calculation of the inverse of the matrix **L** in Eq. (12) is performed, depending solely on material properties, geometry, and boundary conditions, as illustrated in Section 3.3. This step is completed once before the postbuckling analysis begins for efficiency.

5. End shortening and shear strains for each cycle are increased proportionally to those at initial buckling. These strains define the postbuckling analysis and are increased by relative increments of α for each cycle.

6. An approximate amplitude for the trial buckling mode is calculated based on the preceding cycle, assisting the Newton iteration in achieving convergence more efficiently through a modified binary search. For the first cycle, the VICONOPT initial buckling mode is utilized instead.

7 - 9. These steps constitute the in-plane solution of Eq. (12).

10. Since stress redistribution takes place during the postbuckling phase, a new set of longitudinally uniform stress resultants must be determined for each cycle. This step calculates these stress resultants to be equivalent to the current actual distributions, as explained in Section 4.1.

11 - 13. To capture the postbuckling mode in the current cycle, a modified Newton iteration scheme is employed. Further details can be found in Section 4.2.

14. Solutions from the above steps are tabulated.

In Figure 5, The red lines represent the stages involving in-plane solutions, while the yellow ones represent those related to the modified Newton iteration scheme.

3.2. Equivalent uniform stress resultants

Stress redistributions occur due to changes to the mode at each postbuckling cycle. The loading condition at each node also changes with stress redistribution. Historically, the analysis has been simplified by the assumption of effective uniform stress resultants for both compressive and shear loading [27,28]. Here, an energy approach is utilized to approximate the actual stress distributions using stress resultants which are uniform in the longitudinal direction but take different values in each longitudinal strip.

In the context of the buckling analysis, the Kinetic energy by the external loading at node *i* can be formulated by

$$V_i = V_{xi} + V_{yi} + V_{xyi} \tag{17}$$

where the components of V_i are written as

$$V_{xi} = \int_0^L N_{xi}\varepsilon_{xi}dx\,;\; V_{yi} = \int_0^L N_{yi}\varepsilon_{yi}dx\,;\; V_{xyi} = \int_0^L N_{xyi}\gamma_{xyi}dx \tag{18}$$

where the actual stress resultants and strains are obtained from

$$N_{xi} = \sum_{n=0}^{\infty}\left(N_{xi,n,c}\cos\frac{n\pi x}{L} + N_{xi,n,s}\sin\frac{n\pi x}{L}\right); N_{yi} = \sum_{n=0}^{\infty}\left(N_{yi,n,c}\cos\frac{n\pi x}{L} + N_{yi,n,s}\sin\frac{n\pi x}{L}\right)$$
$$; N_{xyi} = \sum_{n=0}^{\infty}\left(N_{xyi,n,c}\cos\frac{n\pi x}{L} + N_{xyi,n,s}\sin\frac{n\pi x}{L}\right) \tag{19}$$

$$\varepsilon_{xi} = \sum_{m=0}^{\infty}\left(\varepsilon_{xi,m,c}\cos\frac{m\pi x}{L} + \varepsilon_{xi,m,s}\sin\frac{m\pi x}{L}\right); \varepsilon_{yi} = \sum_{m=0}^{\infty}\left(\varepsilon_{yi,m,c}\cos\frac{m\pi x}{L} + \varepsilon_{yi,m,s}\sin\frac{m\pi x}{L}\right)$$
$$; \gamma_{xyi} = \sum_{m=0}^{\infty}\left(\gamma_{xyi,m,c}\cos\frac{m\pi x}{L} + \gamma_{xyi,m,s}\sin\frac{m\pi x}{L}\right) \tag{20}$$

where the subscripts m and n are wavelength counts and the s and c represent resulting coefficients from sine and cosine terms, respectively.

Equivalent longitudinally uniform stress resultants $\bar{N}_{xi}$, $\bar{N}_{yi}$ and $\bar{N}_{xyi}$ are now defined under the assumption that they do the same work as the actual stress resultants N_{xi}, N_{yi} and N_{xyi}.

$$\bar{N}_{xi}\int_0^L \varepsilon_{xi}dx = V_{xi};\ \bar{N}_{yi}\int_0^L \varepsilon_{yi}dx = V_{yi};\ \bar{N}_{xyi}\int_0^L \gamma_{xyi}dx = V_{xyi} \tag{21}$$

Substituting Eqs. (21) - (23) into Eq. (24) gives

$$\bar{N}_{xi} = \frac{\int_0^L \sum_{n=0}^{\infty}\sum_{m=0}^{\infty}\left(N_{xi,n,c}\cos\frac{n\pi x}{L} + N_{xi,n,s}\sin\frac{n\pi x}{L}\right)\left(\varepsilon_{xi,m,c}\cos\frac{m\pi x}{L} + \varepsilon_{xi,m,s}\sin\frac{m\pi x}{L}\right)dx}{\int_0^L \sum_{m=0}^{\infty}\left(\varepsilon_{xi,m,c}\cos\frac{m\pi x}{L} + \varepsilon_{xi,m,s}\sin\frac{m\pi x}{L}\right)dx}$$

$$\bar{N}_{yi} = \frac{\int_0^L \sum_{n=0}^{\infty}\sum_{m=0}^{\infty}\left(N_{yi,n,c}\cos\frac{n\pi x}{L} + N_{yi,n,s}\sin\frac{n\pi x}{L}\right)\left(\varepsilon_{yi,m,c}\cos\frac{m\pi x}{L} + \varepsilon_{yi,m,s}\sin\frac{m\pi x}{L}\right)dx}{\int_0^L \sum_{m=0}^{\infty}\left(\varepsilon_{yi,m,c}\cos\frac{m\pi x}{L} + \varepsilon_{yi,m,s}\sin\frac{m\pi x}{L}\right)dx} \tag{22}$$

$$\bar{N}_{xyi} = \frac{\int_0^L \sum_{n=0}^{\infty}\sum_{m=0}^{\infty}\left(N_{xyi,n,c}\cos\frac{n\pi x}{L} + N_{xyi,n,s}\sin\frac{n\pi x}{L}\right)\left(\gamma_{xyi,m,c}\cos\frac{m\pi x}{L} + \gamma_{xyi,m,s}\sin\frac{m\pi x}{L}\right)dx}{\int_0^L \sum_{m=0}^{\infty}\left(\gamma_{xyi,m,c}\cos\frac{m\pi x}{L} + \gamma_{xyi,m,s}\sin\frac{m\pi x}{L}\right)dx}$$

Hence, the stress resultants that are uniform in the longitudinal direction are determined at the level of each node for the ongoing cycle. To derive the equivalent stress resultants to be applied to a specific strip, denoted as i, the average of these values at node i and node i+1 is computed. These averaged stress resultants are a trial applied load for the subsequent cycle.

3.3. Newton Iteration Scheme

The NIS was firstly introduced to assist postbuckling in [2]. Its primary objective is to achieve precise convergence concerning the critical buckling load and the corresponding mode, effectively addressing the transcendental eigenvalue problem which emerges when solving the following equations:

$$\mathbf{K}\,\mathbf{D} = \mathbf{0} \tag{23}$$

where $\mathbf{D} = \{D_j; j = 1, \ldots n\}$ represents the mode of the plate using vectors, encompassing displacements and rotations at longitudinal edges. $\mathbf{K} = \{K_{ij}; i, j = 1, \ldots n\}$ is intricately intertwined with transcendental functions

reliant on the stress resultants within each strip, thereby making it dependent on **D** as well. It is worth noting that while **K** and **D** possess finite orders denoted by n, the approach efficiently preserves an infinite number of internal degrees of freedom due to the exact solution of the governing differential equations for strips. Assume that

$$\mathbf{D} = \mathbf{D}^* + \mathbf{d} \tag{24}$$

where $\mathbf{D}^*$ represents a trial vector for the mode while $\mathbf{d} = \{d_j; j = 1, \dots n\}$ signifies necessary adjustments to $\mathbf{D}^*$ to satisfy Eq. (26). The NIS can be presented in matrix form as follows:

$$\left(\mathbf{K}^* + \sum_{j=1}^{n} \frac{\partial \mathbf{K}^*}{\partial D_j} d_j\right) (\mathbf{D}^* + \mathbf{d}) = \mathbf{0} \tag{25}$$

where $\mathbf{K}^* = \mathbf{K}(\mathbf{D}^*)$. Disregarding higher orders, Eq. (28) simplifies to

$$\sum_{j=1}^{n} \left(K_{ij}^* + \sum_{k=1}^{n} \frac{\partial K_{ik}^*}{\partial D_j} D_k^*\right) d_j = -\sum_{j=1}^{n} K_{ij}^* D_j^* \qquad (i = 1, \dots n) \tag{26}$$

Eq. (29) is solved to determine the adjustment **d**. Upon substitution into Eq. (27), a new trial vector **D** is derived. This new **D** is employed as $\mathbf{D}^*$ in the subsequent iteration. To compute the derivatives required by Eq. (29), finite difference approximations are employed. These approximations involve making small perturbations around the trial values $D_j = D_j^*$. It is essential to note, when an element D_j is perturbed, only derivatives of the plate (or, in certain boundary conditions, strips) directly adjacent to D_j will have non-zero values, and this consideration is accounted for in the computer coding logic.

Because in-plane solutions require more half-wavelengths for precise representation of sophisticated mode shapes, matrices **D** and **K** in Eq. (29) are k times larger compared than the ones from the previous NIS. These matrices need to be constructed using complex arithmetic. Achieving convergence in both the amplitude and mode shape, vector **D** implies convergence on the corrections to the stress resultants caused by flexure. This convergence ensures accurate calculation of the out-of-plane displacements for every postbuckling cycle.

The NIS's convergence is determined by comparing the maximum displacement adjustments in vector **d** with the maximum values in the previous trial mode vector $\mathbf{D}^*$. Convergence is considered reached if the following equation is achieved:

$$\frac{|max(\mathbf{d}) - max\ (\mathbf{D}^*)|}{max\ (\mathbf{D}^*)} \leq \beta \tag{27}$$

where β is the convergence criterion (typically set as 0.001), and $\mathbf{D}^*$ and $\mathbf{d}$ represent the displacements from the last iteration and the displacement adjustments, respectively. Once convergence is achieved, the postbuckling mode for a specific iteration can be determined. In contrast to the previous NIS, the proposed one precisely represents skewed mode shapes emerging from shear load or material anisotropy.

4. Illustrative Results

The examples in this section include composite plates loaded in compression, combined loading and shear. These plates are modelled subjected to different longitudinal boundary conditions, including free, straight, and fixed boundary conditions. All models involve square plates with sides of length 300mm and thickness 2mm, manufactured from materials having properties taken from Zhang [24], $E_{11} = 131kNmm^{-2}$, $E_{12} = 6.41kNmm^{-2}$, $E_{22} = 13kNmm^{-2}$, $G_{12} = G_{13} = G_{23} = 6.41kNmm^{-2}$, $v = 0.38$. Details of the load and boundary conditions along with the orientation of the shear loading and lamination are given in Figure 6 (this lay-up orientation is consistently applied to all structures). The laminates all consist of 16 plies each 0.125mm thick. Three types of laminates with different layups were investigated including case 1: $[0/0/+45/0/-45/0/90/90]_s$, case 2: $[0/-45/+45/0/-45/0/90/90]_s$ and case 3 $[0/90/+45/0/-45/0/90/90/90/0/-45/-45/0/0/+45]_s$, covering balanced symmetric, unbalanced symmetric and unbalanced unsymmetric laminates.

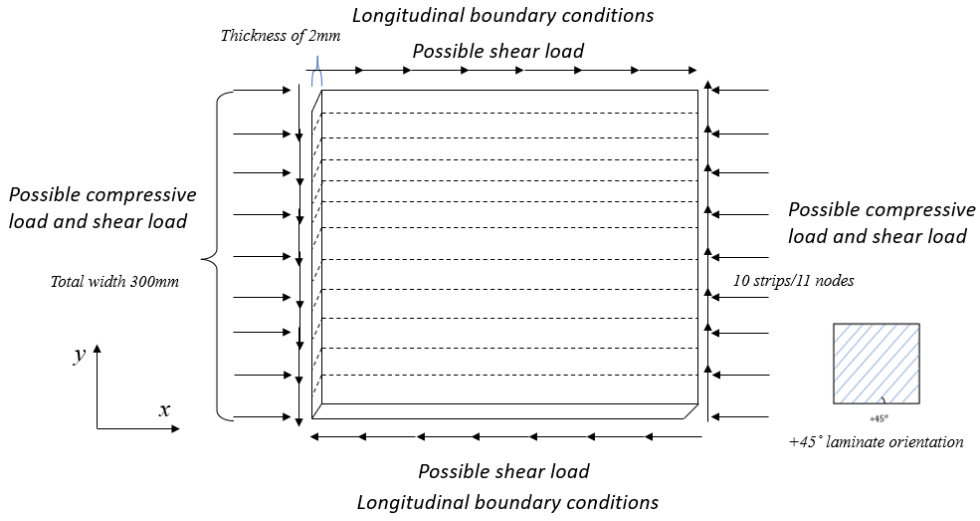

Figure 6. Postbuckling analysis model: in-plane boundary and loading conditions.

Before initiating the analysis, the necessary predefined parameters are selected. For laminates subjected to compression and combined loading, it is sufficient to select three out-of-plane half-wavelengths *l*/(1,3,5) for both

balanced and unbalanced cases. As per Eq. (1) and Eq. (2), this choice results in in-plane displacements that can be represented by combinations of summations *l*/(2,4,6,8,10) and subtractions *l*/(0,2,4), thereby *l*/(0,1,2,3,4,5,6,8,10) [25]. For the pure shear case, five out-of-plane half-wavelengths are needed to adequately represent the swiftly changing mode shapes. For 300 mm plates, configurations with 10 strips (11 nodes) are deemed satisfactory. Regarding the ratio of the end shortening strain increment, a value of 10% is chosen for compression analysis. However, for shear analysis, where capturing the changing buckling modes is more critical, this ratio is reduced to 5%. To perform the analysis effectively, a total of 10 cycles is conducted, and a tolerance level of 0.1% is set for β in the NIS, where β has been found to be small enough to converge on acceptable solutions with no convergence problems. All illustrative examples are initially analysed using VICONOPT to determine the buckling mode for the first cycle of the first iteration of the postbuckling analysis.

To validate CWPAN, a comparison is made with ABAQUS/Standard Solver (ABAQUS Manual Version 6.11) for critical buckling and postbuckling behaviour. In ABAQUS, the panel is simulated using S4R shell elements. A rigorous mesh convergence study was performed under shear load to determine the optimal mesh density for accurate results while maintaining computational efficiency, as shown in Figure 7. As demonstrated in the convergence plot, the maximum stress values stabilize at approximately 427.6 MPa beyond 400 elements. The relative difference between successive mesh refinements drops below 0.03% when increasing from 400 to 625 elements, indicating satisfactory convergence. The 400-element mesh, resulting in 2646 DOFs, was therefore selected as optimal, providing computational efficiency without compromising result accuracy. Stress resultants and strain are computed at the mid-surface of the plate. To compute the eigenvalues, a linear buckling perturbation method is employed with the lowest positive eigenvalue and its associated buckling mode chosen to analyse the postbuckling. A geometric imperfection sensitivity analysis was conducted to ensure the robustness of the ABAQUS benchmark solutions. Initial imperfections were introduced based on the shape of the first linear buckling mode, as it represents the most critical flaw pattern. The amplitude of this imperfection was systematically varied from 0.05% to 1.0% of the laminate thickness. The results indicated that the critical buckling load was particularly sensitive for the laminate under pure shear, where the solution stabilized with a minimal imperfection amplitude of 0.1% of the thickness (0.001 mm). For other loading cases, a slightly larger imperfection of 0.2% (0.002 mm) was required to achieve a consistent and mesh-independent postbuckling path. The final selected imperfection values were used in all subsequent benchmark analyses to provide reliable, conservative results that account for the inevitable minor geometric flaws in real structures, thereby strengthening the validation basis for the CWPAN methodology. Following this, a non-linear analysis is performed using the

Riks method with a 0.01 increment. The Riks method is a numerical technique suitable for solving geometrically nonlinear static problems, including those involving buckling or collapse when the load-displacement response exhibits negative stiffness, indicating that the structure needs to release strain energy to maintain equilibrium.

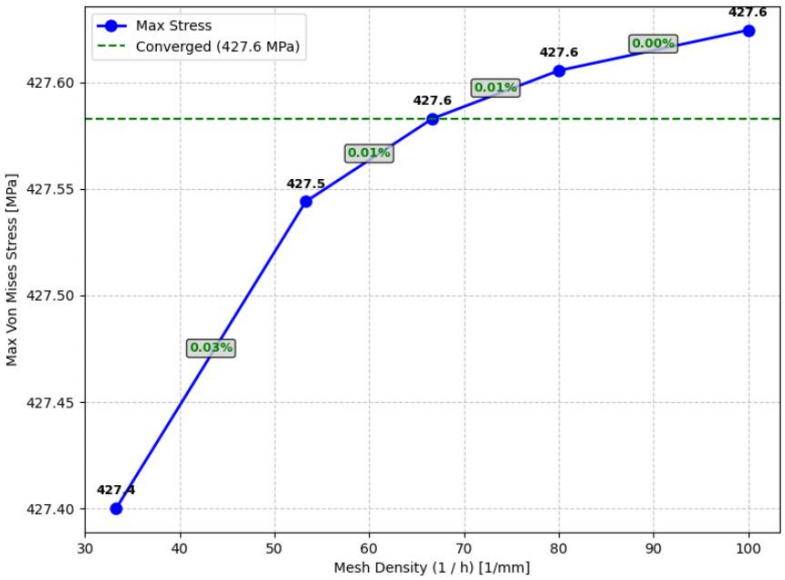

Figure 7. Mesh convergence study (annotations show relative difference %)

4.1. Composite plate loaded in compression

To validate the results for a composite plate with configurations of case 1 subjected to compression with free edges in CWPAN, comparisons are made with results obtained by Zhang [29] and ABAQUS. It is important to note that, in CWPAN, postbuckling is governed by end shortening strain incremented by α in every subsequent postbuckling cycle. ABAQUS analyses are conducted under displacement control for the purpose of comparison.

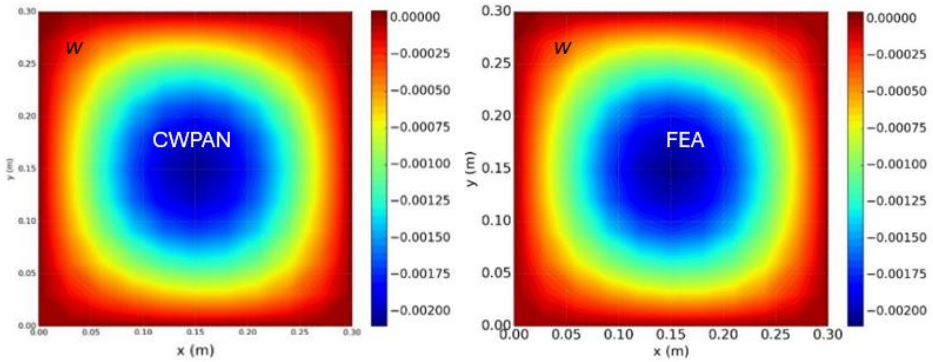

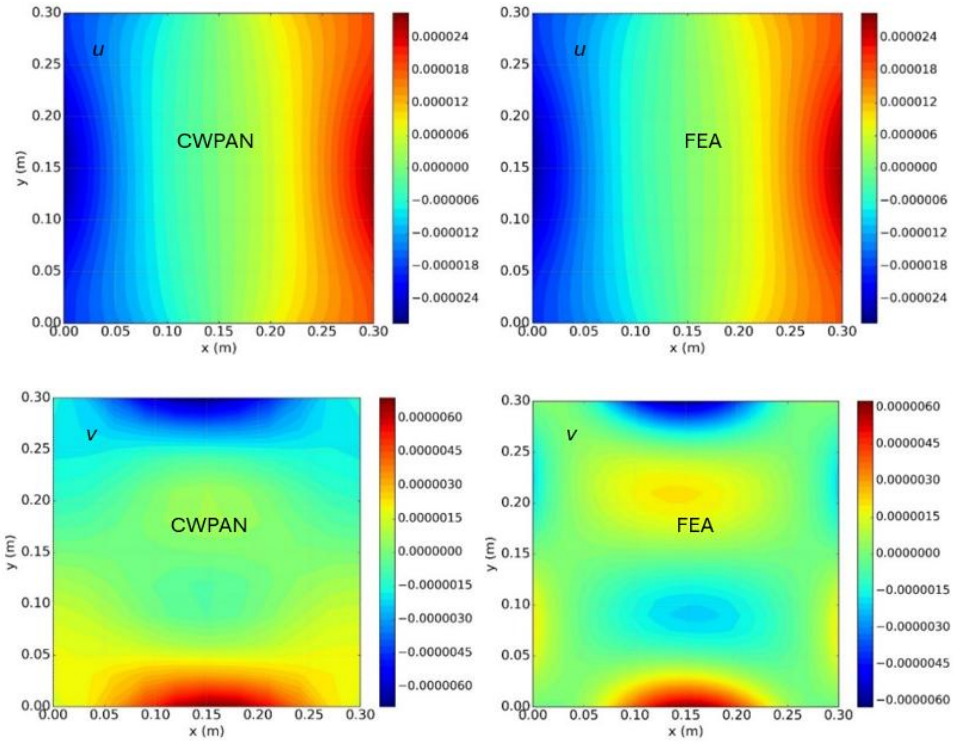

Figure 8. Displacements (m) of the plate subjected to compression, free boundary condition.

Figure 8 provides a comparison of the out-of-plane and in-plane displacements between CWPAN at cycle 8, specifically at 1.8 times of the strain at the initial buckling, which aligns with the case by [30]), and FEA. The comparison between the figures reveals a satisfactory agreement both in terms of shape and numerical values.

Figures 9 compares the stress distributions derived by CWPAN, the peer study by Zhang [29], and the FEA. The solutions by Zhang, as evident from explicit expressions, represents the postbuckling modes by employing five in-plane half-wavelengths. In contrast, CWPAN employs ten half-wavelengths, making it closer to the actual solution. In cases with a low level of anisotropy, such as the one presented here, the differences between the two methods are minimal and negligible. However, for scenarios involving higher levels of anisotropy, as well as under shear loading, CWPAN exhibits improved agreement with the actual solutions which will be illustrated in the subsequent sections.

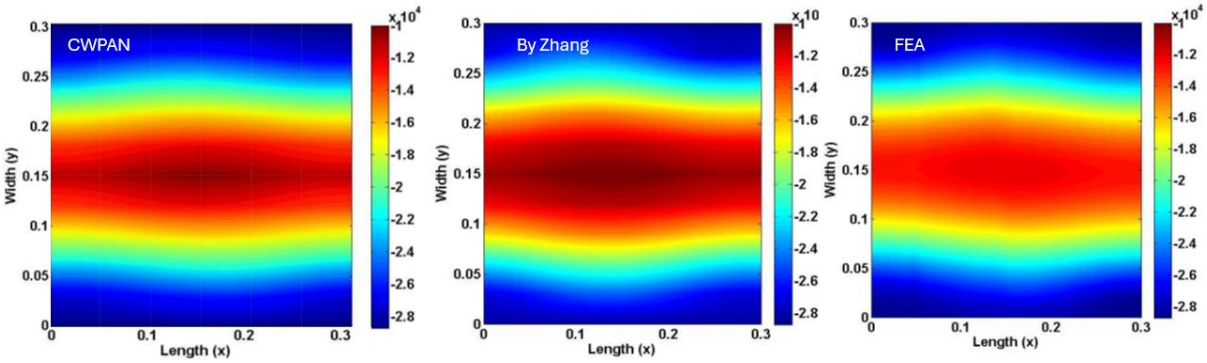

Figure 9. Stress distribution N_x (N/m) of the plate subjected to compression, free boundary condition.

Figure 10 illustrates the maximum lateral deflection against external load calculated by CWPAN in comparison to the FEA solution, with details of the maximum relative difference of only 6.68%. This discrepancy arises because the free boundary conditions on the transverse edges cannot be easily modelled in ABAQUS without inducing rigid body motion, whereas CWPAN addresses this limitation by introducing point supports along the longitudinal strips, as described in Section 2.4. Despite this modelling challenge, the ABAQUS FEA model was constructed to match the CWPAN model as closely as possible, resulting in the relatively small difference reported. This stands in contrast to the peer study by Zhang, where differences of up to 40% were observed, particularly at the centre of the plate [29].

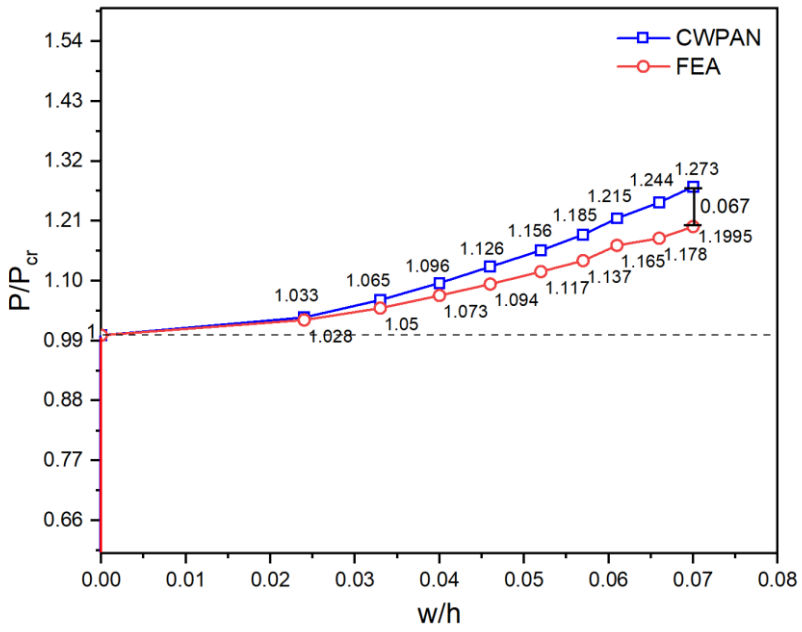

Figure 10. Non-dimensional external compression (P/P_{cr}) vs maximum deflection (w/h).

4.2. Composite plate under pure shear

The investigation of buckling and postbuckling of composite plates with configurations of case 1 under pure shear has received considerable attention in research [13,30,31]. However, most numerical methods lead to prohibitively low computational efficiency or encounter convergence issues because of the substantial nonlinearity involved. The method presented in this paper offers an efficient means of analysing composite plates subjected to pure shear, effectively addressing convergence problems by providing analytical solutions to equilibrium equations.

A plate subjected to pure shear under fixed edges is simulated using CWPAN and verified using ABAQUS. Figures 11 shows the displacement distributions at cycle 5, equivalent to 125% of the initial shear strain (resulting from a 5% strain increment over 5 cycles). These figures demonstrate a close match with the results obtained from an ABAQUS Riks analysis.

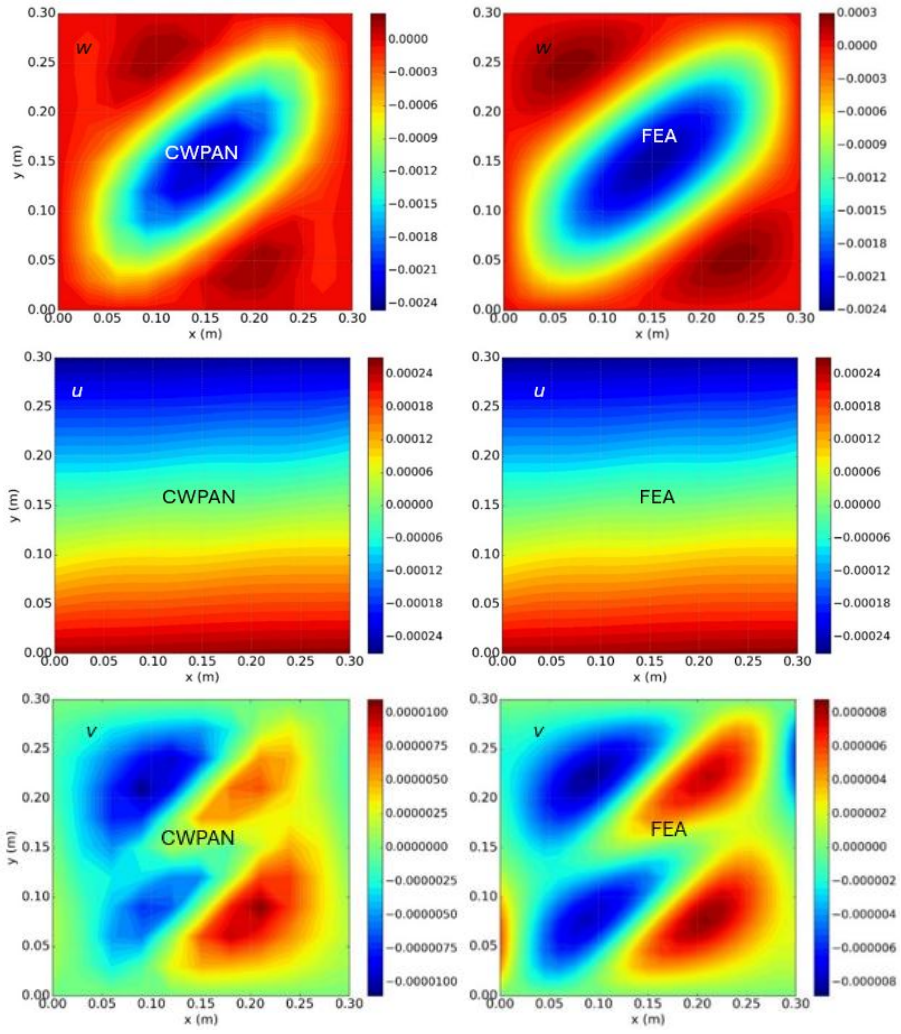

Figure 11. Contours of displacements for plate under shear, fixed boundary conditions.

The CWPAN uses the initial buckling analysis derived from VICONOPT [32], which is based on the assumption that the plate is of infinite length, and the end supports repeat with longitudinal intervals equivalent to the panel length l. Consequently, the buckling mode is also assumed to replicate itself longitudinally with intervals of $L = 2l/\xi$, where ξ is a value that falls within the range 0 to 1. It involves a sequence of responses defined by half-wavelengths expressed as $l/(\xi + 2m)$, where m can assume any integer value and changes for each distinct ξ value.

The benefit of adopting the assumption of infinitely long plates in CWPAN inherits from the VICONOPT analysis, i.e. the intricacy of analysing a single or multiple bays in a panel remains unchanged. This is a significant difference to finite element analysis (FEA). Moreover, within the context of CWPAN, the utilization of the infinitely long plate guarantees that moment equilibrium is maintained between adjacent bays, i.e. in areas where there is continuity with other portions of a larger structure. As a result, this approach offers a closer representation of aircraft wings featuring intermediate transverse stiffeners, like ribs [33].

4.3. Composite plate under combined loading

The composite structure with configuration of case 1 is the applied load consists of a combination of compression and shear, with the shear load having half the magnitude compared to the initial buckling as shown in Figure 6. The additional shear forces lead to more skewing of the mode shape, resulting in more rapid changes in deformation compared to the pure compression case. This skewing results from the non-dominant terms in the sinusoidal solution becoming more significant. Specifically, coefficients associated with non-zero in-plane half-wavelengths become more influential, whereas those for half-wavelength 0 remain dominant. From a structural perspective, shear loading introduces antisymmetry into the system, leading to skewed mode shapes. The results validate the capability of CWPAN to analyse such cases, which cannot be effectively handled by the any ESM-based postbuckling analysis [29].

Figure 12 demonstrates that it is behaving as expected: the displacements, denoted as u, exhibit an approximately linear distribution along the longitudinal direction. This phenomenon can be attributed to the end shortening strain to which the plate is subjected throughout postbuckling analysis, as outlined in Eq. (2). Whilst the Twisting of the contour is caused by nonlinear components arise from the postbuckling stiffness of the structure.

Figure 13 provides an illustrative representation of the longitudinal stresses and shear stresses during the buckling and postbuckling stages. Notably, the figure reveals that during the initial stages of loading, the ratio between the

compressive and shear stresses stands at 0.5. However, as the loading progresses to the later stages, this ratio begins to increase. This phenomenon can be attributed to the anisotropic nature of the composite material, which influences the stress distribution within the structure.

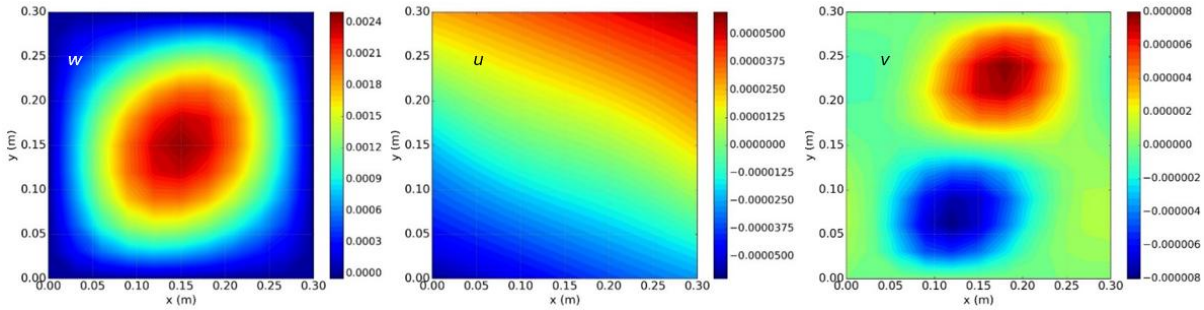

Figure 12. Contour plots of: a. displacements w (m); b. displacements u (m); c. displacements v (m) of plate under pure shear and fixed boundary condition

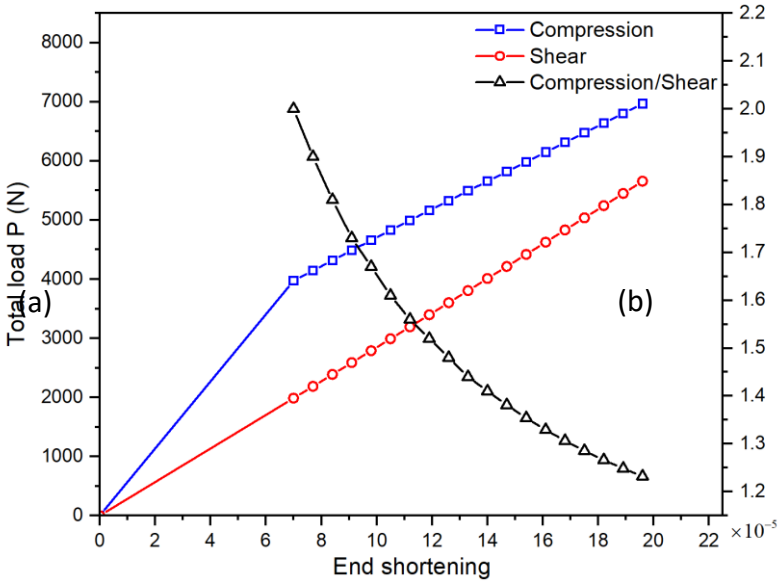

Figure 13. Load path of external shear and compressive load for plate subjected to combined load with fixed condition.

This example of combined loading emphasizes a fundamental difference between the Riks method or arclength method and CWPAN. The arclength method achieves equilibrium by simultaneously increasing applied load and displacements [34]. This implies, in a Riks step, that the external load is always directly proportional to a reference load, i.e. when this load involves combined compression and shear instead of a single force, the ratio between the two individual loads remains constant at all equilibrium states. In contrast, the CWPAN controls the increment at

each cycle based on strain, ensuring that the ratio between increments remains constant rather than the applied forces themselves. As a result, the applied forces do not maintain the same proportion as the initial external load. Hence, comparing the CWPAN with the Riks method in this example is not meaningful.

Figure 14 shows the contour plots of *v* displacements under free edges, fixed edges and straight edges. Since the boundary conditions in-plane are exclusively enforced along the longitudinal edges, the contours of *v* displacements on those boundaries differs significantly. It is evident that the *v* displacements are constrained to be fixed along the longitudinal edges, resulting in two distinct patterns in the upper and lower sections of the plate. Moreover, these contours exhibit motion in opposite directions, reflecting the unique response imposed by this specific boundary condition. Figure 15 presents the load paths for each of the boundary conditions.

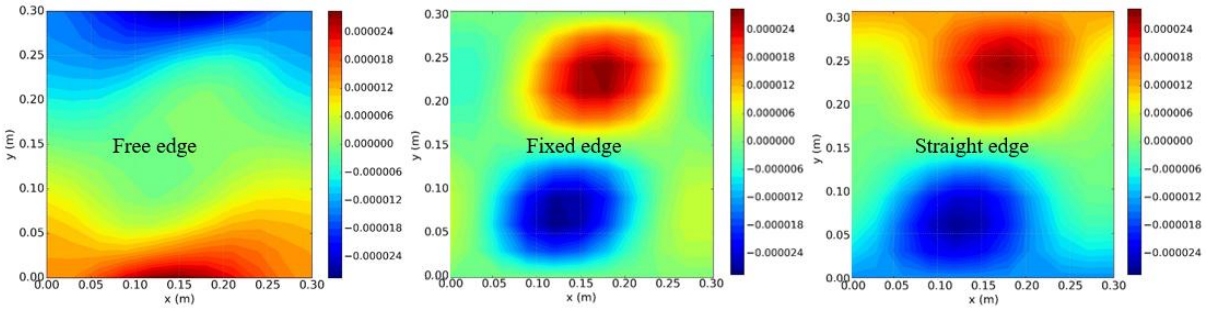

Figure 14. Contour plots of v displacements under different boundary conditions for plate under pure shear.

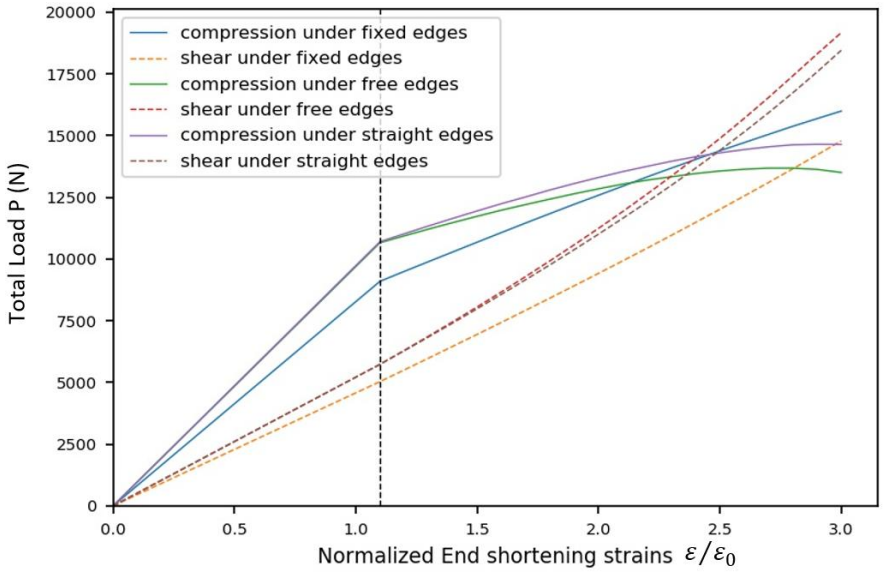

Figure 15. Load paths for the boundary conditions.

4.4. Unbalanced and Unsymmetric Laminates

The modelling of unbalanced symmetric laminates (case 2) is employed to demonstrate the effectiveness of CWPAN in analysing more diverse scenarios. In cases involving unbalanced composite structures, there is a coupling effect between shear and extension during both the buckling and postbuckling phases. This is evident in the stiffness matrix where the terms A_{16} and A_{26} become non-zero, resulting in extra shear strain γ_{xy} induced by stresses N_x and N_y and extra elongations induced by the twist N_{xy} causes.

The unsymmetric laminates (case 3) introduce an added layer of complexity to the postbuckling analysis. This complexity arises from the coupling between out-of-plane curvatures, which encompass twist $\boldsymbol{\kappa}_{xy}$, and bending moments $\mathbf{M}$. Additionally, due to non-zero stiffness elements B_{ij} coupling in plane and out of plane effects, stresses N_x, N_y, N_{xy} induce curvatures, while bending moments M_x, M_y, M_{xy} lead to in-plane strains. To ensure accurate postbuckling analysis, it is essential to incorporate these coupling effects in the expressions for curvatures and moments. During the solution of these equilibrium equations i.e. Eq. (8) and Eq. (9), it becomes apparent that curvatures are exclusively linked to out-of-plane deflections, which are treated as constants derived from the right-hand side of the formulations, while moments M_x, M_y, M_{xy} have no relevance to these equations.

The equivalent shear stress resultants in the transverse direction for the first 20 postbuckling cycles are displayed for the case 2 in Figure 16. The graph reveals fluctuating features, with positive peaks at both ends and negative peaks at the quarter points. Regarding the total shear stress, a notable phenomenon is shown in Figure 17 where the shear stresses do not increase immediately after buckling, primarily because the shear external loads are not imposed at the start of the analysis. Instead, they begin to emerge and continue to rise when the first postbuckling cycle finishes. Structurally, these effects can be attributed to the influence of stiffness elements A_{16} and A_{26} which lead to in-plane stress resultants N_x and N_y inducing twist κ_{xy}, and N_{xy} inducing elongations.

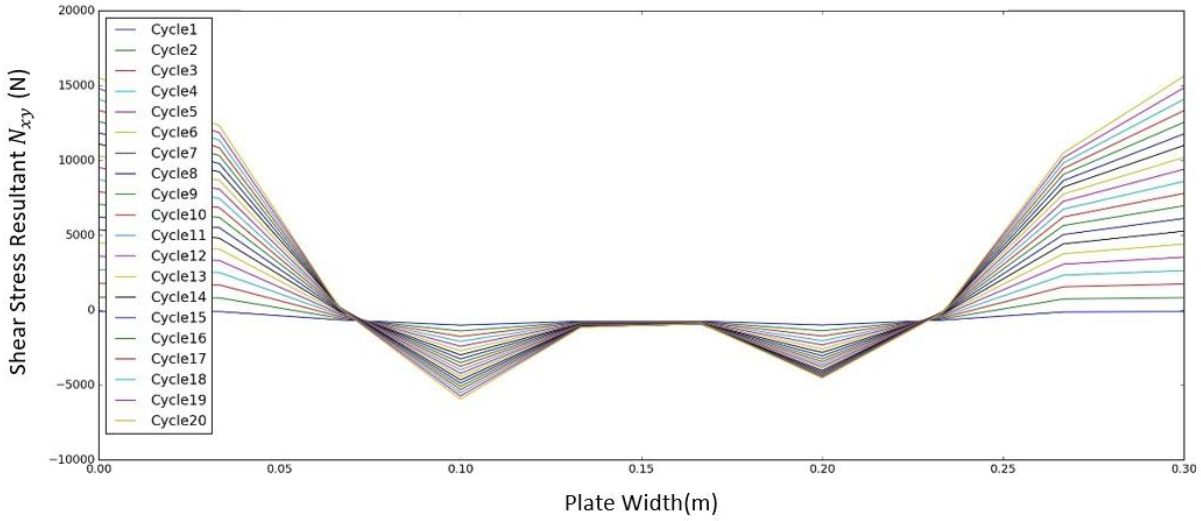

Figure 16. Distribution of equivalent shear stress in the transverse direction for 20 postbuckling cycles for case 2

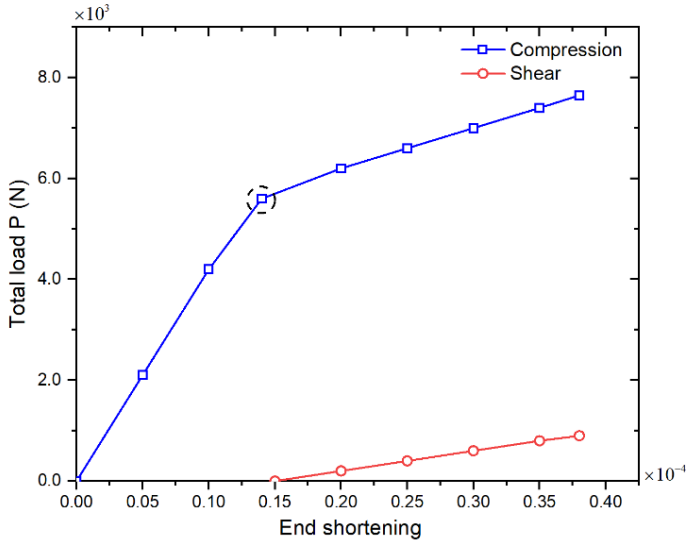

Figure 17. External loads vs end shortening for unbalanced composite subjected to compression.

4.5. Discussion on computational efficiency

The ability to reduce computational time for composite modelling is especially advantageous in aerospace preliminary design. In this context, numerous design scenarios must be investigated, and optimization tasks would traditionally consume months to complete using conventional FEA. In such cases, the importance of a fast and reliable technique cannot be overstated.

The most time-consuming computational task within CWPAN involves solving equilibrium equations, which consist of a number of linear equations. Unlike the FEA, as displacements are represented by sinusoidal terms,

511 the DOFs of CWPAN is associated with number of strips and a series of trigonometric terms rather than nodes.
512 For out-of-plane displacements, the DOFs are 2 (w and ψ) multiplied by the number of nodes multiplied by the
513 number of half-wavelengths used. Similarly, for the in-plane, the DOFs are 2 (u and v) multiplied by the number
514 of nodes multiplied by the number of terms used in the series, i.e. sine and cosine terms for each λ, as shown in
515 Eq. (1) and Eq. (2). To optimize the computational efficiency of CWPAN while maintaining solution accuracy,
516 a comprehensive convergence study on the most extreme case (shear loading and fixed edges) was conducted
517 investigating both the number of strips and the number of half-wavelengths. The computational cost analysis
518 reveals a clear trade-off between accuracy and efficiency. The results, presented in Figure 18, demonstrate that
519 the deflection solution converges rapidly with increasing strip discretization. The model achieves sufficient
520 accuracy with approximately 10 strips, beyond which the reduction in solution error becomes negligible with less
521 than 0.1% change in deflection values.

522 As shown in Figure 19, the execution time increases polynomially with the increasing number of half-wavelengths.
523 This relationship is expected given that the total DOFs scale multiplicatively with these parameters. Based on this
524 convergence study, an optimal configuration of 10 strips with a maximum of 5 half-wavelength terms were
525 selected for all analyses, providing an optimal balance between computational efficiency and numerical accuracy
526 in this study.

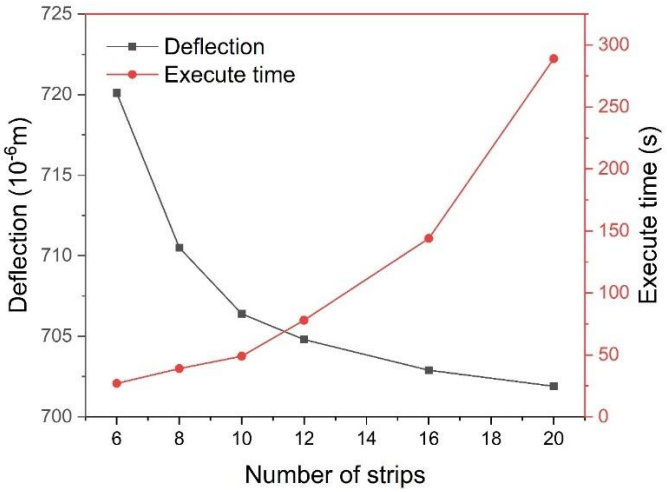

527

528 Figure 18. Convergence study on number of strips based on composite plate under shear load and fixed edges

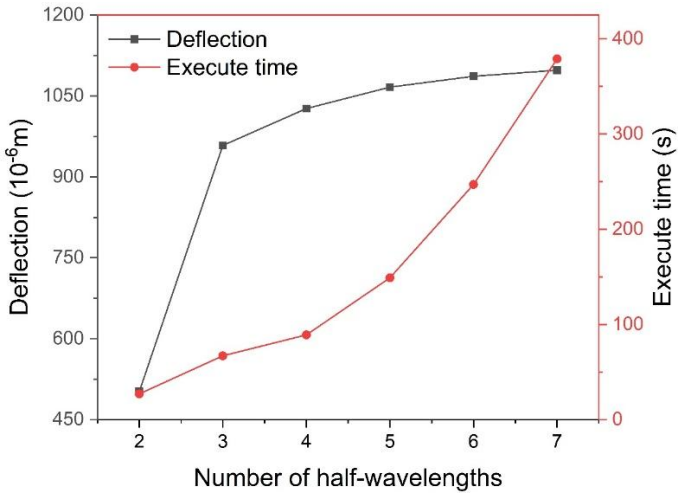

Figure 19. Convergence study on number of half-wavelengths based on composite plate under combined load and fixed edges

A comparative analysis of computational efficiency was conducted between CWPAN and the ABAQUS benchmark. For a model with 10 strips and 5 half-wavelengths (440 DOFs), a single equilibrium iteration in CWPAN requires approximately 0.7 minutes on a standard 4-core i7 computer. The complexity of the stress state influences the solver's convergence, with non-pure shear cases requiring a maximum of 2 iterations per load step, while the more complex pure shear case requires up to 8 iterations. This results in total postbuckling analysis times of approximately 6 minutes and 14 minutes, respectively, to reach 150% of the applied strain. In contrast, an equivalent ABAQUS model discretized with 400 elements (2646 DOFs) required approximately 10 minutes and 18 minutes to complete a similar analysis for the non-shear and shear cases, respectively. This comparison demonstrates that CWPAN achieved a comparable level of accuracy with a 30% reduction in execution time for the most computationally demanding (shear) case, despite the analysis being performed on a system with an 83% smaller number of primary degrees of freedom.

However, a direct comparison of these absolute times is less meaningful than an analysis of the underlying computational scalability. The primary advantage of CWPAN is that its computational complexity, governed by the number of strips and half-wavelengths, remains largely independent of the structure's length due to the underlying periodic assumption. In contrast, the cost of a traditional FEA simulation scales significantly with structural length, as the number of nodes and elements must increase to maintain mesh quality. Therefore, while

549 CWPAN demonstrates moderate efficiency gains for the specific panel analyzed, its computational benefit
550 becomes more significant for the analysis of very long, slender structures, for which it was specifically designed.

551 5. Conclusions

552 In this paper, a coupled wavelength postbuckling analysis is presented, which offers an efficient and dependable
553 method for academia and industry to investigate postbuckling behaviours in composite laminates subjected to
554 various in-plane loadings. Built upon the ESM, the underlying theory of CWPAN analysis postbuckling of
555 composite laminates using coupled trigonometric functions and the governing equations can be solved analytically
556 at each strip. In order to apply this approach effectively in postbuckling analysis, an overall convergence
557 framework including effective uniform stress resultants calculations, buckling amplitude calculations and the NIS,
558 is proposed to track gradual changes in out-of-plane displacements. By incorporating postbuckling stiffness, these
559 techniques ensure the accurate capture of out-of-plane displacements during postbuckling. Validation experiments
560 have been conducted to compare the CWPAN with the Riks method in the ABAQUS. The solutions successfully
561 mirror postbuckling phenomena, providing validation for the method. The method demonstrates the capability to
562 accurately predict the displacement distributions both in- and out-of-plane along the postbuckling path.

563 The proposed CWPAN method offers several key advantages over conventional FEA for specific applications.
564 First, it accurately captures the complex, highly skewed postbuckling modes of composite laminates under shear
565 loading, which are often challenging to model. Second, a key efficiency gain is achieved for slender, high-aspect-
566 ratio structures like aircraft fuselages and wings. By modeling the structure as periodically long, the computational
567 cost of CWPAN is independent of the physical length, maintaining a constant number of DOFs, unlike FEA where
568 cost escalates. Finally, the strip-based formulation generates a smaller global stiffness matrix with fewer DOFs,
569 resulting in lower computational cost. While the method's formulation can be conceptually extended to other
570 shapes, such as circular or asymmetric panels, by adding constraints, this requires further investigation on the
571 accuracy and computational efficiency for these generalized cases.

572 However, the CWPAN has the limitations that the stiffened panels cannot be analysed. This is because as the half-
573 wavelengths for the in-plane displacements are generalized from the out-of-plane displacements, they naturally
574 cannot be represented by the same set. However, for stiffened panels, the skins' out-of-plane displacements are
575 the stiffeners' in-plane displacements and vice versa. This cannot be achieved in explicit expressions for the
576 current method. As a result, the method cannot model the core load-carrying mechanism in stiffened panels, where
577 the coupling of skin and stiffener deformations is critical. This limits the method's direct utility for designing and

optimizing lightweight aerospace structures, which rely heavily on stiffened panel configurations. The future work will focus on extending the CWPAN by representing the in-plane and out-of-plane displacements with one set of half-wavelengths.

The presented research establishes the baseline performance of the CWPAN for ideal structures. Future research will also focus on enhancing its practical relevance and broadening its application. This will involve introducing both general and localized geometric imperfections to rigorously evaluate the method's sensitivity and reliability in predicting the collapse of as-manufactured components. Furthermore, the framework will be extended to model severe nonlinear instabilities, including snap-through and snap-back phenomena, to fully capture the complex post-buckling response of thin-walled structures.

References

[1] Z. Wu, G. Raju, P. Weaver, Analysis and design for the moderately deep postbuckling behavior of composite plates, Journal of Aircraft 54 (2017) 327–335.

[2] M. Anderson, D. Kennedy, Postbuckling of composite stiffened panels using exact strip analysis with Newton iteration, in: 49th AIAA/ASME/ASCE/AHS/ASC Structures, Structural Dynamics, and Materials Conference, 16th AIAA/ASME/AHS Adaptive Structures Conference, 10th AIAA Non-Deterministic Approaches Conference, 9th AIAA Gossamer Spacecraft Forum, 4th AIAA Multidisciplinary Des, (2008): p. 2184.

[3] K. Abu Salem, V. Cipolla, G. Palaia, V. Binante, D. Zanetti, A physics-based multidisciplinary approach for the preliminary design and performance analysis of a medium range aircraft with box-wing architecture, Aerospace 8 (2021). https://doi.org/10.3390/aerospace8100292.

[4] D. Kennedy, C.A. Featherston, Exact strip analysis and optimum design of aerospace structures, The Aeronautical Journal 114 (2010) 505–512.

[5] V.P. Nguyen, C. Anitescu, S.P.A. Bordas, T. Rabczuk, Isogeometric analysis: an overview and computer implementation aspects, Math Comput Simul 117 (2015) 89–116.

[6] T.J.R. Hughes, J.A. Cottrell, Y. Bazilevs, Isogeometric analysis: CAD, finite elements, NURBS, exact geometry and mesh refinement, Comput Methods Appl Mech Eng 194 (2005) 4135–4195.

[7] J. Xu, Q. Zhao, P. Qiao, A critical review on buckling and post-buckling analysis of composite structures, Frontiers in Aerospace Engineering 2 (2013) 157.

[8] F. Ebrahimi, E. Salari, A semi-analytical method for vibrational and buckling analysis of functionally graded nanobeams considering the physical neutral axis position, CMES: Comput. Model. Eng. Sci 105 (2015) 151–181.

[9] C. Bisagni, R. Vescovini, Analytical formulation for local buckling and post-buckling analysis of stiffened laminated panels, Thin-Walled Structures 47 (2009) 318–334. https://doi.org/10.1016/j.tws.(2008_.07.006.

[10] C. Bisagni, R. Vescovini, Fast tool for buckling analysis and optimization of stiffened panels, J Aircr 46 (2009) 2041–2053. https://doi.org/10.2514/1.43396.

[11] R. Vescovini, C. Bisagni, Buckling analysis and optimization of stiffened composite flat and curved panels, AIAA Journal 50 (2012) 904–915.

[12] G. Raju, Z. Wu, P.M. Weaver, Postbuckling analysis of variable angle tow plates using differential quadrature method, Compos Struct 106 (2013) 74–84. https://doi.org/10.1016/j.compstruct.2013.05.010.

[13] G. Raju, Z. Wu, P.M. Weaver, Buckling and postbuckling of variable angle tow composite plates under in-plane shear loading, Int J Solids Struct 58 (2015) 270–287. https://doi.org/10.1016/j.ijsolstr.2015.01.011.

[14] Q. Chen, P. Qiao, Buckling and postbuckling of rotationally-restrained laminated composite plates under shear, Thin-Walled Structures 161 (2021). https://doi.org/10.1016/j.tws.2021.107435.

[15] Z. Wang., X. Chen, B. Wang, Y. Huang, and P. Chen, Analysis and experimental evaluation framework for buckling and post-buckling of composite stiffened panels. *Journal of Composite Materials*, *59*(1) (2025), pp.99-117.

[16] N. Bouslama, A. Maslouhi, and P. Masson, , Experimental and numerical investigation of damage evolution in carbon fiber reinforced polymer stiffened panel in post-buckling regime. *Journal of Composite Materials*, *56*(15) (2022), pp.2455-2470.

[17] T. Shojaee, B. Mohammadi, M. Pourhosseinshahi and I. Zeydabadi, Buckling and post-buckling analysis of composite laminates with cutout under compressional loading based on the first-order shear deformation theory. *Acta Mechanica*, *234*(5) (2023), pp.2145-2165.

[18] W.H. Wittrick, A unified approach to the initial buckling of stiffened panels in compression, Aeronautical Quarterly 19 (1968) 265–283.

[19] W. Wittrick, F. Williams, A general algorithm for computing natural frequencies of elastic structures, Q J Mech Appl Math 24 (1971) 263–284.

[20] W.H. Wittrick, F.W. Williams, Buckling and vibration of anisotropic or isotropic plate assemblies under combined loadings, Int J Mech Sci 16 (1974) 209–239.

[21] F.W. Williams, M.S. Anderson, Incorporation of Lagrangian multipliers into an algorithm for finding exact natural frequencies or critical buckling loads, Int J Mech Sci 25 (1983) 579–584.

[22] D. Kennedy, F.W. Williams, and M.S. Anderson, Buckling and vibration analysis of laminated panels using VICONOPT. Journal of Aerospace Engineering, 7(3) (1994), pp.245-262.

[23] R. Butler, F.W. Williams, Optimum buckling design of compression panels using VICONOPT, Structural Optimization 6 (1993) 160–165.

[24] C. Zhang, Kennedy D, Featherston CA. Improved exact strip postbuckling analysis for anisotropic plates, PhD thesis, (2012).

[25] K. Zhao, D. Kennedy, C.A. Featherston, Exact strip postbuckling analysis of composite plates under compression and shear, Aeronautical Journal 123 (2019) 658–677. https://doi.org/10.1017/aer.2019.27.

[26] S. Levy, P. Krupen, Large-deflection theory for end compression of long rectangular plates rigidly clamped along two edges, (1943).

[27] D.L. von Kármán T, Sechler EE, The strength of Thin Plates in Compression., Transactions of American Society of Mechanical Engineers 54(2) (1932) 53–57.

[28] G. Winter, Strength of thin steel compression flanges, Transactions of the American Society of Civil Engineers 112 (1947) 527–554.

[29] C. Zhang, Postbuckling analysis of isotropic and anisotropic plate assemblies under combined loading, (2018).

[30] Y. Zhang, F.L. Matthews, Postbuckling behavior of anisotropic laminated plates under pure shear and shear combined with compressive loading, AIAA Journal 22 (1984) 281–286.

[31] S.C. Han, S.Y. Lee, G. Rus, Postbuckling analysis of laminated composite plates subjected to the combination of in-plane shear, compression and lateral loading, Int J Solids Struct 43 (2006) 5713–5735. https://doi.org/10.1016/j.ijsolstr.2005.08.004.

[32] D. Kennedy, F.W. Williams, M.S. Anderson, Buckling and Vibration Analysis of Laminated Panels Using VICONOPT, J Aerosp Eng 7 (1994) 245–262. https://doi.org/10.1061/(asce)0893-1321(1994)7:3(245).

[33] C.G. Diaconu, P.M. Weaver, Postbuckling of long unsymmetrically laminated composite plates under axial compression, Int J Solids Struct 43 (2006) 6978–6997. https://doi.org/10.1016/j.ijsolstr.2006.02.017.

[34] B.A. Memon, X.Z. Su, Arc-length technique for nonlinear finite element analysis, J Zhejiang Univ Sci 5 (2004) 618–628. https://doi.org/10.1631/jzus.2004.0618.

Appendix

The matrix that appears in this paper expressed in terms of displacements *u*, *v* and *w*.

Strains that obtained by von Kármán large deflection theory from Eq. (6) can be written as:

$$\begin{bmatrix} \varepsilon_{xi} \\ \varepsilon_{yi} \\ \gamma_{xyi} \\ \kappa_{xi} \\ \kappa_{yi} \\ \kappa_{xyi} \end{bmatrix} = \begin{bmatrix} \dfrac{\partial u_i}{\partial x} + \dfrac{1}{2}\left(\dfrac{\partial w_i}{\partial x}\right)^2 \\ \dfrac{\partial v_i}{\partial y} + \dfrac{1}{2}\left(\dfrac{\partial w_i}{\partial y}\right)^2 \\ \dfrac{\partial u_i}{\partial y} + \dfrac{\partial v_i}{\partial x} + \dfrac{\partial w_i}{\partial x}\dfrac{\partial w_i}{\partial y} \\ -\dfrac{\partial^2 w_i}{\partial x^2} \\ -\dfrac{\partial^2 w_i}{\partial y^2} \\ -2\dfrac{\partial^2 w_i}{\partial x \partial y} \end{bmatrix} = \begin{bmatrix} \varepsilon_{xi0} & \varepsilon_{xi1c} & \varepsilon_{xi1s} & \cdots \\ \varepsilon_{yi0} & \varepsilon_{yi1c} & \varepsilon_{yi1s} & \cdots \\ \gamma_{xyi0} & \gamma_{xyi1c} & \gamma_{xyi1s} & \cdots \\ \kappa_{xi0} & \kappa_{xi1c} & \kappa_{xi1s} & \cdots \\ \kappa_{yi0} & \kappa_{yi1c} & \kappa_{yi1s} & \cdots \\ \kappa_{xyi0} & \kappa_{xyi1c} & \kappa_{xyi1s} & \cdots \end{bmatrix} \begin{bmatrix} 1 \\ \cos\left(\dfrac{\pi x}{\lambda_1}\right) \\ \sin\left(\dfrac{\pi x}{\lambda_1}\right) \\ \cos\left(\dfrac{\pi x}{\lambda_2}\right) \\ \sin\left(\dfrac{\pi x}{\lambda_2}\right) \\ \cos\left(\dfrac{\pi x}{\lambda_3}\right) \\ \sin\left(\dfrac{\pi x}{\lambda_3}\right) \\ \vdots \end{bmatrix} \tag{A1}$$

In Eq. 7, $\mathbf{w}_i$, $\mathbf{u}_i$ and $\boldsymbol{\varepsilon}_i$ can be written as:

$$\mathbf{w}_i = \begin{bmatrix} w_{i1c} \\ w_{i1s} \\ w_{i2c} \\ w_{i2s} \\ \vdots \end{bmatrix}, \mathbf{u}_i = \begin{bmatrix} u_{1,0} \\ u_{1,1c} \\ u_{1,1s} \\ u_{1,2c} \\ \vdots \\ v_{1,0} \\ v_{1,1c} \\ v_{1,1s} \\ v_{1,2c} \\ \vdots \\ u_{2,0} \\ u_{2,1c} \\ u_{2,1s} \\ u_{2,2c} \\ \vdots \\ v_{2,0} \\ v_{2,1c} \\ v_{2,1s} \\ v_{2,2c} \\ \vdots \\ u_{n,0} \\ u_{n,1c} \\ u_{n,1s} \\ u_{n,2c} \\ \vdots \\ v_{n,0} \\ v_{n,1c} \\ v_{n,1s} \\ v_{n,2c} \\ \vdots \end{bmatrix}, \boldsymbol{\varepsilon}_i = \begin{bmatrix} \varepsilon_{x1,0} \\ \varepsilon_{x1,1c} \\ \varepsilon_{x1,1s} \\ \varepsilon_{x1,2c} \\ \vdots \\ \varepsilon_{y1,0} \\ \varepsilon_{y1,1c} \\ \varepsilon_{y1,1s} \\ \varepsilon_{y1,2c} \\ \vdots \\ \gamma_{xy1,0} \\ \gamma_{xy1,1c} \\ \gamma_{xy1,1s} \\ \gamma_{xy1,2c} \\ \vdots \\ \varepsilon_{xn,0} \\ \varepsilon_{xn,1c} \\ \varepsilon_{xn,1s} \\ \varepsilon_{xn,2c} \\ \vdots \\ \varepsilon_{yn,0} \\ \varepsilon_{yn,1c} \\ \varepsilon_{yn,1s} \\ \varepsilon_{yn,2c} \\ \vdots \\ \gamma_{xyn,0} \\ \gamma_{xyn,1c} \\ \gamma_{xyn,1s} \\ \gamma_{xyn,2c} \\ \vdots \end{bmatrix} \boldsymbol{\kappa}_i = \begin{bmatrix} \kappa_{x1,0} \\ \kappa_{x1,1c} \\ \kappa_{x1,1s} \\ \kappa_{x1,2c} \\ \vdots \\ \kappa_{y1,0} \\ \kappa_{y1,1c} \\ \kappa_{y1,1s} \\ \kappa_{y1,2c} \\ \vdots \\ \kappa_{xy1,0} \\ \kappa_{xy1,1c} \\ \kappa_{xy1,1s} \\ \kappa_{xy1,2c} \\ \vdots \\ \kappa_{xn,0} \\ \kappa_{xn,1c} \\ \kappa_{xn,1s} \\ \kappa_{xn,2c} \\ \vdots \\ \kappa_{yn,0} \\ \kappa_{yn,1c} \\ \kappa_{yn,1s} \\ \kappa_{yn,2c} \\ \vdots \\ \kappa_{xyn,0} \\ \kappa_{xyn,1c} \\ \kappa_{xyn,1s} \\ \kappa_{xyn,2c} \\ \vdots \end{bmatrix} \tag{A2}$$

$\mathbf{w}_i$ includes all out-of-plane displacements and rotations; $\mathbf{u}_i$ includes in-plane displacements include longitudinal and transverse displacements; $\boldsymbol{\varepsilon}_i$ include all $\boldsymbol{\varepsilon}_x$, $\boldsymbol{\varepsilon}_y$ and $\boldsymbol{\varepsilon}_{xy}$. i denotes the strip number and subscript 0 is constant terms c and s are amplitudes of cosine terms and sine terms respectively.

Also, in Eq. (7):

$$\boldsymbol{\varepsilon}_1 = \begin{bmatrix} \overline{\boldsymbol{\varepsilon}_1} & \mathbf{0}_{3K,2K} & \dots & \mathbf{0}_{3K,2K} \\ \mathbf{0}_{3K,2K} & \overline{\boldsymbol{\varepsilon}_1} & \dots & \mathbf{0}_{3K,2K} \\ \vdots & \vdots & \ddots & \vdots \\ \mathbf{0}_{3K,2K} & \mathbf{0}_{3K,2K} & \dots & \overline{\boldsymbol{\varepsilon}_1} \end{bmatrix} \tag{A3}$$

$$\boldsymbol{\varepsilon}_2 = \begin{bmatrix} \overline{\boldsymbol{\varepsilon}_2} & \mathbf{0}_{3K,2K} & \dots & \mathbf{0}_{3K,2K} \\ \mathbf{0}_{3K,2K} & \overline{\boldsymbol{\varepsilon}_2} & \dots & \mathbf{0}_{3K,2K} \\ \vdots & \vdots & \ddots & \vdots \\ \mathbf{0}_{3K,2K} & \mathbf{0}_{3K,2K} & \dots & \overline{\boldsymbol{\varepsilon}_2} \end{bmatrix} \tag{A4}$$

$$\overline{\boldsymbol{\varepsilon}_1} = \begin{bmatrix} \mathbf{J} & \mathbf{0}_{2K-1,2K-1} \\ \mathbf{0}_{2K-1,2K-1} & \mathbf{0}_{2K-1,2K-1} \\ \mathbf{0}_{2K-1,2K-1} & \mathbf{J} \end{bmatrix}, \overline{\boldsymbol{\varepsilon}_2} = \begin{bmatrix} \mathbf{0}_{2K-1,2K-1} & \mathbf{0}_{2K-1,2K-1} \\ \mathbf{0}_{2K-1,2K-1} & \mathbf{I}_{2K-1,2K-1} \\ \mathbf{I}_{2K-1,2K-1} & \mathbf{0}_{2K-1,2K-1} \end{bmatrix} \tag{A5}$$

where $\mathbf{I}_{m,m}$ and $\mathbf{0}_{m,n}$ are unit matrix of order (m,m) and zero matrix of order (m,n), respectively. K is the number of unique in-plane half-wavelengths. The coefficient matrix $\mathbf{J}$ is given by

$$\mathbf{J} = \begin{bmatrix} \lambda_1\frac{\pi}{a} & 0 & 0 & 0 & 0 & \dots & 0 & 0 \\ 0 & \lambda_2\frac{\pi}{a} & 0 & 0 & 0 & \dots & 0 & 0 \\ 0 & -\lambda_2\frac{\pi}{a} & 0 & 0 & 0 & \dots & 0 & 0 \\ 0 & 0 & 0 & \lambda_3\frac{\pi}{a} & 0 & \dots & 0 & 0 \\ 0 & 0 & 0 & -\lambda_3\frac{\pi}{a} & 0 & \ddots & 0 & 0 \\ \vdots & \vdots & \vdots & \vdots & \vdots & 0 & 0 & \\ 0 & 0 & 0 & 0 & 0 & 0 & \lambda_K\frac{\pi}{a} & \\ 0 & 0 & 0 & 0 & 0 & -\lambda_K\frac{\pi}{a} & 0 & \end{bmatrix} \tag{A6}$$

690 and the first order finite difference approximation matrix **f** by

$$\boldsymbol{f} = \frac{(n_n - 1)}{2b}\begin{bmatrix} -3\mathbf{I}_{2K,2K} & 4\mathbf{I}_{2K,2k} & -\mathbf{I}_{2K,2k} & \mathbf{0}_{2K,2K} & \mathbf{0}_{2K,2K} & \cdots & \mathbf{0}_{2K,2K} \\ -\mathbf{I}_{2K,2K} & \mathbf{0}_{2K,2K} & \mathbf{I}_{2K,2K} & \mathbf{0}_{2K,2K} & \mathbf{0}_{2K,2K} & \cdots & \mathbf{0}_{2K,2K} \\ \mathbf{0}_{2K,2K} & -\mathbf{I}_{2K,2K} & \mathbf{0}_{2K,2K} & \mathbf{I}_{2K,2K} & \mathbf{0}_{2K,2K} & \cdots & \mathbf{0}_{2K,2K} \\ \mathbf{0}_{2K,2K} & \mathbf{0}_{2K,2K} & -\mathbf{I}_{2K,2K} & \mathbf{0}_{2K,2K} & \mathbf{I}_{2K,2K} & \cdots & \mathbf{0}_{2K,2K} \\ \mathbf{0}_{2K,2K} & \mathbf{0}_{2K,2K} & \mathbf{0}_{2K,2K} & -\mathbf{I}_{2K,2K} & \mathbf{0}_{2K,2K} & \cdots & \mathbf{0}_{2K,2K} \\ \vdots & \vdots & \vdots & \vdots & \vdots & \ddots & \mathbf{0}_{2K,2K} \\ \mathbf{0}_{2K,2K} & \mathbf{0}_{2K,2K} & \mathbf{0}_{2K,2K} & \cdots & -\mathbf{I}_{2K,2K} & \mathbf{0}_{2K,2K} & \mathbf{I}_{2K,2K} \\ \mathbf{0}_{2K,2K} & \mathbf{0}_{2K,2K} & \mathbf{0}_{2K,2K} & \cdots & \mathbf{I}_{2K,2K} & -4\mathbf{I}_{2K,2K} & 3\mathbf{I}_{2K,2K} \end{bmatrix} \tag{A7}$$

691 Similar to strains data structure, stresses can be written as:

$$\boldsymbol{N}_i = \begin{bmatrix} N_{x1,0} \\ N_{x1,1c} \\ N_{x1,1s} \\ N_{x1,2c} \\ \vdots \\ N_{y1,0} \\ N_{y1,1c} \\ N_{y1,1s} \\ N_{y1,2c} \\ \vdots \\ N_{xy1,0} \\ N_{xy1,1c} \\ N_{xy1,1s} \\ N_{xy1,2c} \\ \vdots \\ N_{xn,0} \\ N_{xn,1c} \\ N_{xn,1s} \\ N_{xn,2c} \\ \vdots \\ N_{yn,0} \\ N_{yn,1c} \\ N_{yn,1s} \\ N_{yn,2c} \\ \vdots \\ N_{xyn,0} \\ N_{xyn,1c} \\ N_{xyn,1s} \\ N_{xyn,2c} \\ \vdots \end{bmatrix}, \boldsymbol{M}_i = \begin{bmatrix} M_{x1,0} \\ M_{x1,1c} \\ M_{x1,1s} \\ M_{x1,2c} \\ \vdots \\ M_{y1,0} \\ M_{y1,1c} \\ M_{y1,1s} \\ M_{y1,2c} \\ \vdots \\ M_{xy1,0} \\ M_{xy1,1c} \\ M_{xy1,1s} \\ M_{xy1,2c} \\ \vdots \\ M_{xn,0} \\ M_{xn,1c} \\ M_{xn,1s} \\ M_{xn,2c} \\ \vdots \\ M_{yn,0} \\ M_{yn,1c} \\ M_{yn,1s} \\ M_{yn,2c} \\ \vdots \\ M_{xyn,0} \\ M_{xyn,1c} \\ M_{xyn,1s} \\ M_{xyn,2c} \\ \vdots \end{bmatrix} \tag{A8}$$

$$\mathbf{A} = \begin{bmatrix} \overline{\mathbf{A}} & \mathbf{0}_{6K-3,6K-3} & \dots & \mathbf{0}_{6K-3,6K-3} \\ \mathbf{0}_{6K-3,6K-3} & \overline{\mathbf{A}} & \dots & \mathbf{0}_{6K-3,6K-3} \\ \vdots & \vdots & \ddots & \mathbf{0}_{6K-3,6K-3} \\ \mathbf{0}_{6K-3,6K-3} & \mathbf{0}_{6K-3,6K-3} & \mathbf{0}_{6K-3,6K-3} & \overline{\mathbf{A}} \end{bmatrix} \tag{A9}$$

$$\overline{\mathbf{A}} = \begin{bmatrix} A_{11} * \mathbf{0}_{2K-1,2K-1} & A_{12} * \mathbf{0}_{2K-1,2K-1} & A_{16} * \mathbf{0}_{2K-1,2K-1} \\ A_{21} * \mathbf{0}_{2K-1,2K-1} & A_{22} * \mathbf{0}_{2K-1,2K-1} & A_{26} * \mathbf{0}_{2K-1,2K-1} \\ A_{61} * \mathbf{0}_{2K-1,2K-1} & A_{62} * \mathbf{0}_{2K-1,2K-1} & A_{66} * \mathbf{0}_{2K-1,2K-1} \end{bmatrix} \tag{A10}$$

where $\mathbf{0}_{6K-3}$ is a zero matrix with the same size as $\overline{\mathbf{A}}$

$$\overline{\mathbf{B}} = \begin{bmatrix} B_{11} * \mathbf{0}_{2K-1,2K-1} & B_{12} * \mathbf{0}_{2K-1,2K-1} & B_{16} * \mathbf{0}_{2K-1,2K-1} \\ B_{21} * \mathbf{0}_{2K-1,2K-1} & B_{22} * \mathbf{0}_{2K-1,2K-1} & B_{26} * \mathbf{0}_{2K-1,2K-1} \\ B_{61} * \mathbf{0}_{2K-1,2K-1} & B_{62} * \mathbf{0}_{2K-1,2K-1} & B_{66} * \mathbf{0}_{2K-1,2K-1} \end{bmatrix}, \tag{A11}$$

$$\mathbf{B} = \begin{bmatrix} \overline{\mathbf{B}} & \mathbf{0}_{6K-3,6K-3} & \cdots & \mathbf{0}_{6K-3,6K-3} \\ \mathbf{0}_{6K-3,6K-3} & \overline{\mathbf{B}} & \cdots & \mathbf{0}_{6K-3,6K-3} \\ \vdots & \vdots & \ddots & \mathbf{0}_{6K-3,6K-3} \\ \mathbf{0}_{6K-3,6K-3} & \mathbf{0}_{6K-3,6K-3} & \mathbf{0}_{6K-3,6K-3} & \overline{\mathbf{B}} \end{bmatrix} \tag{A12}$$

$$\overline{\mathbf{D}} = \begin{bmatrix} D_{11}\mathbf{0}_{2K-1,2K-1} & D_{12}\mathbf{0}_{2K-1,2K-1} & D_{16}\mathbf{0}_{2K-1,2K-1} \\ D_{21}\mathbf{0}_{2K-1,2K-1} & D_{22}\mathbf{0}_{2K-1,2K-1} & D_{26}\mathbf{0}_{2K-1,2K-1} \\ D_{61}\mathbf{0}_{2K-1,2K-1} & D_{62}\mathbf{0}_{2K-1,2K-1} & D_{66}\mathbf{0}_{2K-1,2K-1} \end{bmatrix}, \tag{A13}$$

$$\mathbf{D} = \begin{bmatrix} \overline{\mathbf{D}} & \mathbf{0}_{6K-3,6K-3} & \cdots & \mathbf{0}_{6K-3,6K-3} \\ \mathbf{0}_{6K-3,6K-3} & \overline{\mathbf{D}} & \cdots & \mathbf{0}_{6K-3,6K-3} \\ \vdots & \vdots & \ddots & \mathbf{0}_{6K-3,6K-3} \\ \mathbf{0}_{6K-3,6K-3} & \mathbf{0}_{6K-3,6K-3} & \mathbf{0}_{6K-3,6K-3} & \overline{\mathbf{D}} \end{bmatrix} \tag{A14}$$

694 In Eq. (10), ***s*** is the matrix of second order derivative of stresses respect to *y* direction

$$\mathbf{s} = \frac{(n_n-1)^2}{b^2} \begin{bmatrix} 2*\mathbf{I}_{2K,2K} & -5*\mathbf{I}_{2K,2K} & 4*\mathbf{I}_{2K,2K} & -1*\mathbf{I}_{2K,2K} & \mathbf{0}_{2K,2K} & \cdots \\ 1*\mathbf{I}_{2K,2K} & -2*\mathbf{I}_{2K,2K} & -1*\mathbf{I}_{2K,2K} & \mathbf{0}_{2K,2K} & \mathbf{0}_{2K,2K} & \cdots \\ \mathbf{0}_{2K,2K} & 1*\mathbf{I}_{2K,2K} & -2*\mathbf{I}_{2K,2K} & -1*\mathbf{I}_{2K,2K} & \mathbf{0}_{2K,2K} & \cdots \\ \mathbf{0}_{2K,2K} & \mathbf{0}_{2K,2K} & 1*\mathbf{I}_{2K,2K} & -2*\mathbf{I}_{2K,2K} & -1*\mathbf{I}_{2K,2K} & \cdots \\ \mathbf{0}_{2K,2K} & \mathbf{0}_{2K,2K} & \mathbf{0}_{2K,2K} & 1*\mathbf{I}_{2K,2K} & -2*\mathbf{I}_{2K,2K} & \cdots \\ \vdots & \vdots & \vdots & \vdots & \vdots & \ddots \\ \mathbf{0}_{2K,2K} & \mathbf{0}_{2K,2K} & \mathbf{0}_{2K,2K} & \mathbf{0}_{2K,2K} & \mathbf{0}_{2K,2K} & 1*\mathbf{I}_{2K,2K} \\ \mathbf{0}_{2K,2K} & \mathbf{0}_{2K,2K} & \mathbf{0}_{2K,2K} & \mathbf{0}_{2K,2K} & -1*\mathbf{I}_{2K,2K} & 4*\mathbf{I}_{2K,2K} \end{bmatrix} \tag{A15}$$

$$\begin{bmatrix} \mathbf{0}_{2K,2K} & \mathbf{0}_{2K,2K} \\ \mathbf{0}_{2K,2K} & \mathbf{0}_{2K,2K} \\ \mathbf{0}_{2K,2K} & \mathbf{0}_{2K,2K} \\ \mathbf{0}_{2K,2K} & \mathbf{0}_{2K,2K} \\ \mathbf{0}_{2K,2K} & \mathbf{0}_{2K,2K} \\ \mathbf{0}_{2K,2K} & \mathbf{0}_{2K,2K} \\ -2*\mathbf{I}_{2K,2K} & -1*\mathbf{I}_{2K,2K} \\ -5*\mathbf{I}_{2K,2K} & 2*\mathbf{I}_{2K,2K} \end{bmatrix}$$

695 In Eq. (13) and (14)

$$\overline{\mathbf{T}} = \begin{bmatrix} \mathbf{0}_{2K-1,2K-1} & \mathbf{0}_{2K-1,2K-1} & \mathbf{I}_{2K-1,2K-1} \\ \mathbf{0}_{2K-1,2K-1} & \mathbf{I}_{2K-1,2K-1} & \mathbf{0}_{2K-1,2K-1} \end{bmatrix}, \tag{A16}$$

$$\overline{\mathbf{R}} = \begin{bmatrix} \mathbf{J} & \mathbf{0}_{2K-1,2K-1} & \mathbf{0}_{2K-1,2K-1} \\ \mathbf{0}_{2K-1,2K-1} & \mathbf{0}_{2K-1,2K-1} & \mathbf{J} \end{bmatrix}, \tag{A17}$$

$$\mathbf{T} = \begin{bmatrix} \overline{\mathbf{T}} & \mathbf{0}_{3K,2K} & \dots & \mathbf{0}_{3K,2K} \\ \mathbf{0}_{3K,2K} & \overline{\mathbf{T}} & \dots & \mathbf{0}_{3K,2K} \\ \vdots & \vdots & \ddots & \mathbf{0}_{3K,2K} \\ \mathbf{0}_{3K,2K} & \mathbf{0}_{3K,2K} & \mathbf{0}_{3K,2K} & \overline{\mathbf{T}} \end{bmatrix}, \tag{A18}$$

$$\mathbf{R} = \begin{bmatrix} \overline{\mathbf{R}} & \mathbf{0}_{3K,2K} & \dots & \mathbf{0}_{3K,2K} \\ \mathbf{0}_{3K,2K} & \overline{\mathbf{R}} & \dots & \mathbf{0}_{3K,2K} \\ \vdots & \vdots & \ddots & \mathbf{0}_{3K,2K} \\ \mathbf{0}_{3K,2K} & \mathbf{0}_{3K,2K} & \mathbf{0}_{3K,2K} & \overline{\mathbf{R}} \end{bmatrix} \tag{A19}$$

696